# *Chapter-4*

# Delignification of biomass for *in-situ* synthesis of $MoS_2$ for dye remediation

**Motivation**

*In this chapter, we aim to mitigate the issues related to the mismanagement of agricultural residues and stubble burning. We focus on using rice husk and sugarcane bagasse as carriers for the in-situ growth of* $MoS_2$ *via the hydrothermal method and converting them into value-added catalyst forms for the remediation of dyes and pollutants.*

- ***Global challenges***

***Stubble burning:*** *Stubble burning, and mismanagement of crop residues a common agricultural practice in India, results in air pollution, deteriorates soil health, causing respiratory issues.*

***Environmental Threat:*** *The indiscriminate release of synthetic dyes such as Methylene blue and Malachite green and microbiological contaminants poses a severe threat to terrestrial and aquatic ecosystems and increases the risk to human health.*

- ***The solution addressed in this chapter***

***Utilization of Agricultural Waste:*** *Sugarcane bagasse (SB) and rice husk (RH), as untapped sources of agricultural waste, are chosen as carriers for the in-situ synthesis of catalysts.*

***Targeted Contaminants:*** *The focus is on remediating methylene blue dye, malachite green dye, and microbiological contaminants generally found in real wastewater.*

***Simultaneous dye and microbial decontamination:*** $MoS_2$*, due to its photocatalytic activity, helped in the photodegradation of dyes and inactivation of bacteria in wastewater.*

***The work in this chapter is published as:***

1. *Ranjan, R., Bhatt, S. B., Rai, R., Sharma, S. K., Verma, M., & Dhar, P. (2024). Valorization of sugarcane bagasse with in situ grown $MoS_2$ for continuous pollutant remediation and microbial decontamination. Environmental Science and Pollution Research, 1-17.*
2. *Ranjan, R., Bhatt, S. B., Rai, R., Sharma, S. K., Ranjan, R., Bharti, A., & Dhar, P. (2024). Rice husk valorisation by in situ grown $MoS_2$ nanoflowers: a dual-action catalyst for pollutant dye remediation and microbial decontamination. RSC advances, 14(17), 12192-12203.*

## Graphical abstract

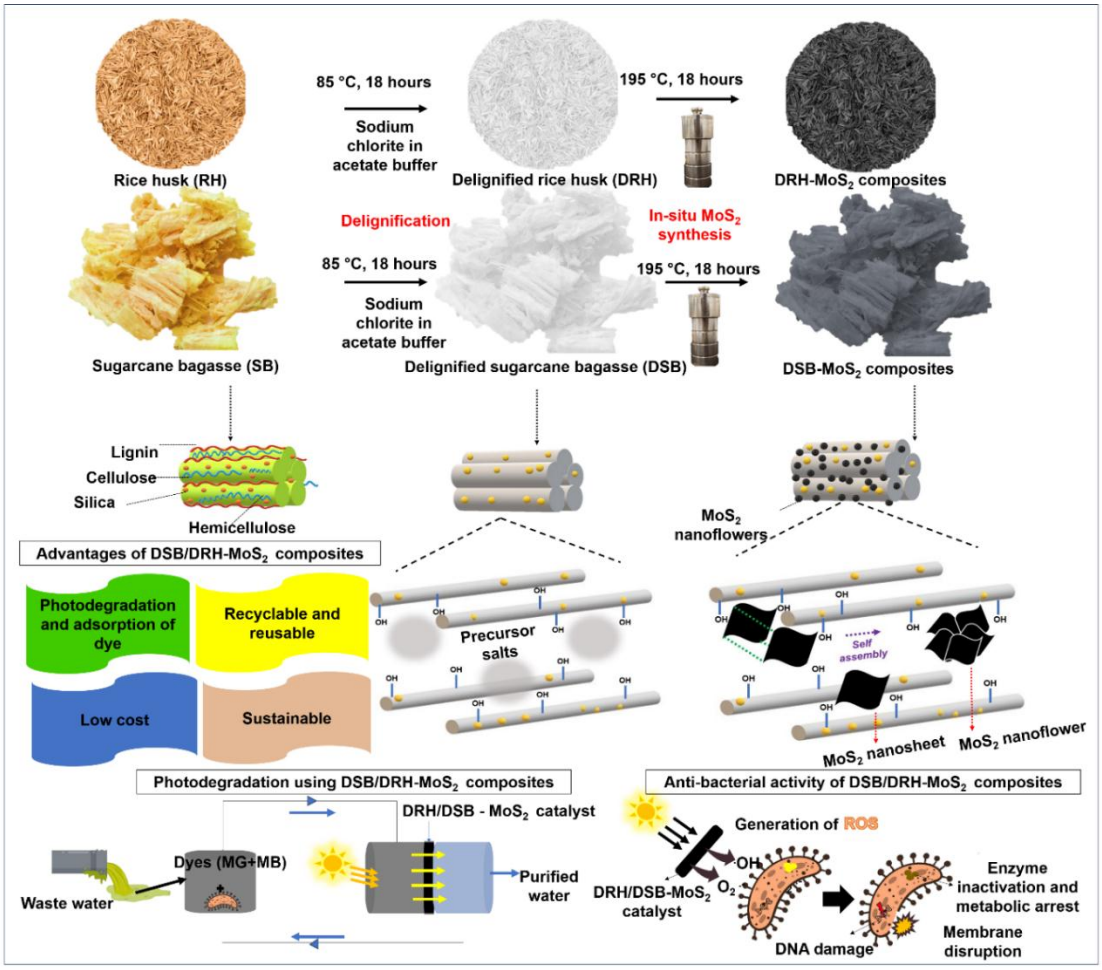

## 4.1 Introduction

The deterioration of the air, aquatic, and soil ecosystems has increased significantly due to global industrialization. Textiles, printing, leather, cosmetics, and electroplating industry emits a large number of organic dyes such as methyl orange, MB, azo dyes, and rhodamine B, which inflict long-term damage to ecosystems and human beings [334,335]. Due to the toxicity associated with dyes, their removal from industrial waste effluent is necessary. Multiple chemical processes such as oxidation, photocatalysis, biological oxidation, and adsorption have been utilized to degrade organic contaminants such as dyes [336]. However, the high cost and scalability of these technologies are a major concern [337]. Adsorption as an alternative approach is a low-cost, convenient, and scalable process that can be utilized on a large scale to remove organic dyes [338]. Multiple adsorbents have been developed for the adsorption and removal of organic dyes based on metal oxides [339], clays [340], biochar [341], activated carbon [342], and metal-organic frameworks (MOF) [343] have been reported in the literature.

Sugarcane, as one of the primary sources of natural commercial sugars, is widely cultivated in tropical and subtropical regions, especially in Brazil (20.57 %), India (16.91 %), and China (6.31 %). India generates about 19.2 million tons of sugar from 571 sugar mills, making it the second-largest sugar-producing country [344]. Once sugarcane juice is extracted by crushing, the fibrous remains form part of SB, which is generated in large amounts as industrial waste (~100 million tons annually), the disposal of which poses a huge challenge to the environment [345]. SB is primarily composed of cellulose (32-45 %), lignin (17-32 %), hemicellulose (20-32 %), and ash (1-9 %), each of which has unique properties with potential applications [346].

As one of the most produced and consumed crops, rice feeds more than 40 % of the world's population, which, however, results in the generation of large amounts of waste globally (~ 731 MT of rice straws and ~160 MT of RH [347]. India is a major agriculture-based economy, and rice is the major crop with an annual yield of 124 MT tons, generating ~20 % of the crop portion as RH waste [348]. RH is an abundantly available by-product from the rice milling industry, with an annual production of 120 million tons with limited applications [349]. It has been used as animal feed but has challenges due to its poor nutritional value [350], high fibre content [351], and allergic effects in digestive tract [352]. RH has a tough, water-insoluble matrix composed of cellulose-silica structures with the composition of cellulose (~35 %), hemicellulose (~25 %), lignin (~20 %), and ash with a silica content of ~15-20 % [353]. RH is highly porous and lightweight due to high ash content with a bulk density of 96-160 kg/$m^3$ and 75-90 % organic matter. The exterior part of RH is made of dentate rectangular elements of silica with thick cuticles and surface hairs [354]. RH generated from the processing of rice grains is usually disposed of by landfill, drastically increasing the aesthetic pollution, eutrophication, and perturbations in the aquatic ecosystems and organisms. Due to its high volume, RH is difficult to handle through proper waste management. It is generally subjected to uncontrolled burning, which generates ashes, contributing to air pollution and global greenhouse gas emissions. Due to high accumulation and potential ecological toxicity, strategies for using RH biomass for innovative applications are the current need of the hour.

It has been applied abundantly for paper making, sustainable packaging, and biofuel production to resolve the accumulation of SB and RH waste [355]. In recent years, SB has also been utilized for the development of lignophenolic thermoset

composites [356], transportation infrastructure applications [357], particleboard panels [358], disposable utensils [50], biochar for cotton production in rainfed areas [359], filler materials [360], particulate matter removal [361], interior cladding fiberboard [362], aerogel for solar desalination [363] and so on. Similarly, due to its low cost, abundance, high porosity, functionality, and surface area, RH makes it a suitable substrate as a high-performance adsorbent for removing carcinogenic pollutants, dye, and heavy metals. RH waste has been applied for a plethora of applications, such as pest control [32], fertilisers [33], insulators [34], construction [35], catalysts [36], and adsorbents[364]. However, due to the high-volume generation of SB and RH waste, it is still dumped through landfilling or burned uncontrollably. The SB and RH contribute to the release of environmentally detrimental gaseous pollutants, including carbon monoxide (CO), nitrogen oxides ($NO_x$), and carbon dioxide ($CO_2$). These emissions are considered environmentally harmful, directly affecting respiratory organs and cardiovascular diseases [365]. Therefore, large-scale industrially feasible SB waste processing strategies for its conversion into value-added products through green and sustainable approaches are the need of the hour.

Due to the presence of active catalytic sites, large surface area, photocatalytic, semiconductor, electronic, and optical properties, 2D materials such as molybdenum disulfide ($MoS_2$) have gathered huge attention in the last decade [148]. $MoS_2$ presents a layered 2D structure composed of S-Mo-S moiety linked *via* Van der Waals forces, tunable band structure, and strong adsorption capacity [366]. $MoS_2$, due to its attractive properties, such as visible light adsorption and photocatalytic action *via* electron-hole pair recombination, has been abundantly utilised for the photodegradation of dyes and wastewater pollutants [367]. $MoS_2$ has a band gap of 1.96 eV, making it suitable for visible light absorption and catalysis. Most studies reported in the literature only focus

on the remediation of dyes or pollutants. However, many pathogenic microbial loads remain unprocessed and require additional pre-treatment steps to make water suitable for consumption and reuse. $MoS_2$ generates active free radicals, which mediates the degradation of contaminants and simultaneously forms ROS, which induces antimicrobial properties [368].

Considering above mentioned properties of $MoS_2$, several studies have been performed in last one decade for development of biocatalyst. Gopalakrishnan et al. [369] used a hydrothermal route to develop a hybrid material consisting of a few-layered $MoS_2$ nanosheets on graphene-infused cellulose filter paper. This novel adsorbent was developed to remove MB from solutions and was found to adsorb 485.4 mg/g of MB. Tu et al. [370] prepared functionalized carboxylated loofah with MIL-101(Fe) and $MoS_2$, which shows photodegradation of MB~93.2 % and tetracycline~84.6 % in 24 and 120 minutes, respectively. The developed composite also showed long stability with cyclic photodegradation of MB ~81.99 % even after four cycles. Zhao et al. [151] prepared nanosized $MoS_2$ with nanofibrous cellulose microspheres, which shows the removal of heavy metals ($Pb^{2+}$) by ~80 % and organic dyes (Congo Red) by ~327.6 mg/g. Qiu et al. developed $MoS_2$ into the highly porous structure of cellulose *via* a hydrothermal process for the removal of Congo red (334.92 mg/g) [371]. The *in-situ* formation of *2H*-$MoS_2$ nanoparticles occurred on BC, eliminating MG (100 % for 10 mM) and bacterial disinfection against *E. coli* and *S. aureus* [371]. In a study by Gao et al. created magnetic cellulose microparticles to serve as carriers for the *in-situ* growth of $MoS_2$. The resulting composite demonstrated a peak adsorption capacity of 469.5 mg/g specifically for $Hg^{2+}$ [372]. In a study by Zhao et al., the growth of $MoS_2$ nanoparticles within the nanofibrous structures of porous cellulose led to the adsorption of 327.6 mg/g of $Pb^{+2}$ and the removal of 80 % of Congo red and

MB [373]. Furthermore, the antibacterial properties of the $MoS_2$ have also been extensively studied, which helped in the microbial decontamination of wastewater. Shen et al. [374] investigated a BC-$MoS_2$ composite, demonstrating notable photodegradation activity with 97.5 % reduction in malachite green and exceptional antibacterial properties, achieving a 99.9 % removal of both *S. aureus* and *E. coli*. Shen et al., in another study, developed a composite of BC/$MoS_2$/chitosan, leading to a 99.9 % decrease in *E. coli* and *S. aureus* through photoinactivation when exposed to visible light [152]. Jin et al. engineered a nano-platform targeting multidrug resistance by incorporating polyethyleneimine, $MoS_2$, and zeolitic imidazolate framework-8. This advanced nano-platform demonstrated a remarkable 95 % enhancement in multidrug resistance against *S. aureus* and *E. coli*, concurrently promoting accelerated wound healing in mice with multidrug-resistant infections [375]. In the current work, *in-situ* synthesis of $MoS_2$ nanosheets on DSB and DRH templates for simultaneous absorption and photodegradation of MB dye and microbial decontamination is developed.

SB and RH were strategically delignified to expose the hydroxyl groups on the cellulose surface, followed by hydrothermal treatment for *in-situ* synthesis of $MoS_2$ nanosheets. SB and RH are low-cost, abundantly available, and renewable cellulose sources utilized for uniform growth, distribution, and localization of $MoS_2$ nanosheets inside their microfibrillar structure. Cationic dyes such as MB and MG adsorb on the surface of DSB *via* weak chemical interactions, which are degraded by the photocatalytic activity of $MoS_2$ nanosheets. Under visible light irradiation, $MoS_2$ also generates reactive oxygen species (ROS), which induces antimicrobial characteristics in DRH-$MoS_2$ and DSB-$MoS_2$. Thus, with the current approach, continuous photodegradation of organic dyes and pathogenic micro biota can be achieved simultaneously in industrial waste streams. The developed DRH-$MoS_2$ and DSB-$MoS_2$

composites present a facile, scalable, and low-cost strategy for the valorization of abundantly available SB and RH waste into high-performance biocatalysts for the remediation of chemo-biological pollutants from wastewater, creating a cleaner and safer environment. This chapter is divided into two sections. Section 4.2 discusses the SB, DSB and DSB-$MoS_2$, and section 4.3 discusses RH, DRH and DRH-$MoS_2$.

## 4.2 Results and discussion

SB is an abundant lignocellulosic waste generated by the sugarcane industry worldwide, disposal of which is a major issue; however, it contains cellulose, hemicellulose, and lignin as major components with interesting physio-chemical properties. The delignification of SB wastes results in the exposure of the hydroxyl groups on its surface, forming a porous network that provides sites for the physisorption of MB dye. In current work, DSB has been used as a template for *in-situ* growth of $MoS_2$ nanosheets.

The precursor $MoS_2$ salts localize in the vicinity of cellulosic hydroxyl groups through charge-based interactions, which, on hydrothermal treatment, self-assemblies to form a nanoflower-like structure, as summarized in ***Figure 4.1***. Considering the inherent characteristics of photocatalytic degradation and the anti-bacterial activity of $MoS_2$ nanosheets, the remediation of chemical and biological contaminants of wastewater is studied. $MoS_2$-generated reactive oxygen species (ROS) act on the bacterial membrane and cause damage to its DNA along with protein denaturation. DSB-$MoS_2$ composite was also applied for continuous and simultaneous degradation of MB dye and decontamination, which presents the possibility of valorization of SB biomass for large-scale wastewater treatment facilities.

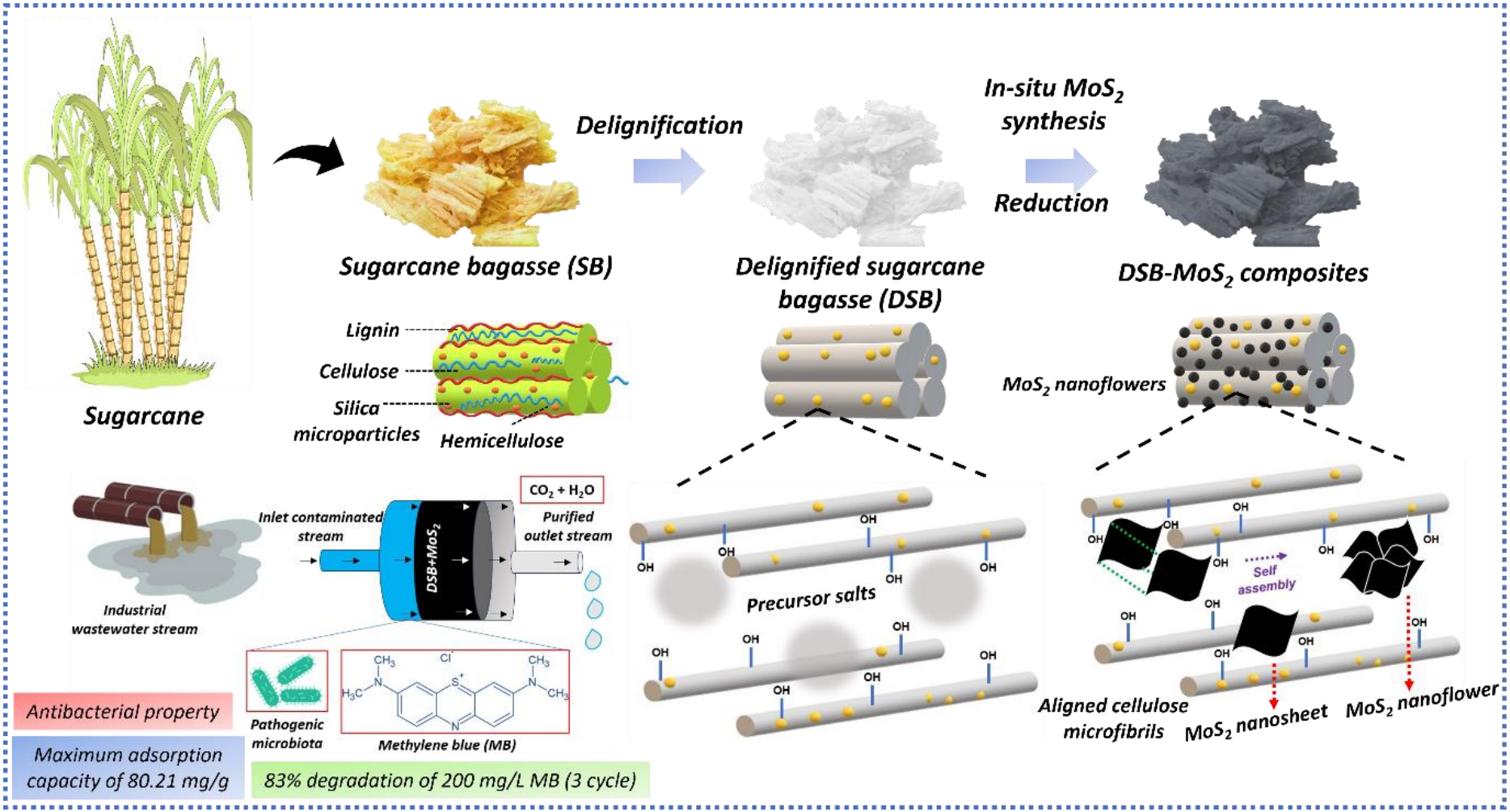


***Figure 4.1*** *Schematic illustration for processing of SB through strategic delignification followed by in-situ growth of $MoS_2$ nanosheets, which self-assembles into nanoflower-like architecture for simultaneous dye adsorption, photodegradation, and microbial decontamination.*

### 4.2.1 Physiochemical and functional properties of DSB and DSB-$MoS_2$

FTIR spectroscopy was used to determine functional groups existing in SB and DSB and to confirm the *in-situ* growth of $MoS_2$ (***Figure 4.2*(a)**). The common peaks of SB, DSB and DSB-$MoS_2$ were detected at 655, 898 and 1107 $cm^{-1,}$ which corresponds to O=C-O bending vibration [376], C-H bending in cellulose [377] and backbone vibration of C–O [378] respectively. The common peaks of SB and DSB were detected at 3404 $cm^{-1}$, 2916 $cm^{-1}$, 1378 $cm^{-1}$,1324 $cm^{-1,}$ 1255 $cm^{-1}$ and 1053 $cm^{-1,}$ which corresponds to stretching of hydroxyl groups [379], -CH stretching vibration [380], bending vibration of C-H [381], carbonyl group (C=O) of aldehyde and ketone [382], C=O bond [383] and O-H group of cellulose [384] respectively. FTIR spectra of SB show the presence of characteristic peaks of 833 $cm^{-1}$, 1161 $cm^{-1}$, 1515 $cm^{-1}$ and 1732 $cm^{-1,}$ which corresponds to C-H out-of-plane bending in phenolic compounds [385], C-O-C asymmetric vibration [386], C=C aromatic skeletal vibration of the aromatic ring in lignin, C−O stretching vibration of hemicellulose and lignin [377] respectively. FTIR spectra of DSB show the absence of lignin peaks corresponding to the aromatic rings (C=C) and the absence of the stretching vibration of lignin (C-O) at 1515 $cm^{-1}$ and 1732 $cm^{-1,}$ respectively, which confirms the successful delignification process. The FTIR spectra of DSB-$MoS_2$ show characteristic peaks at 3425 $cm^{-1}$, 1611 $cm^{-1,}$ ,1399 $cm^{-1}$, 1153 $cm^{-1}$, 1029 $cm^{-1}$ and 594 $cm^{-1}$ which represents -OH stretching vibration [387], hydroxyl (O–H) groups [388], $MoS_2$ nanosheets [389], C-O bond [390], stretching vibration of Mo-O bond [388] and Mo-S bonds [391] respectively. The 665 $cm^{-1}$ and 898 $cm^{-1}$ peaks exhibited greater SB intensity than DSB and DSB-$MoS_2$. Conversely, the peak at 1107 $cm^{-1}$ showed greater intensity in DSB-$MoS_2$ than in SB and DSB. The peaks 1053 $cm^{-1}$, 1255 $cm^{-1}$, 1324 $cm^{-1}$, 1378 $cm^{-1}$, 2916 $cm^{-1}$, and 3404

$cm^{-1}$ displayed a greater intensity in SB than DSB. It is expected that the abundant hydroxyl groups in DSB provide sites for the adsorption of ammonium molybdate salts through charge-based electrostatic interactions, which, on hydrothermal treatment in the presence of thiourea reduced to form $MoS_2$ nanosheets. The FTIR spectra of SB and DSB exhibit peaks at 1053 $cm^{-1}$ and 1255 $cm^{-1}$, which undergo a red shift to 1029 $cm^{-1}$ and 1198 $cm^{-1,}$ respectively, as a result of the *in-situ* growth of $MoS_2$ on DSB (DSB-$MoS_2$). Additionally, the distinctive peak at 1638 $cm^{-1}$ in the FTIR spectra of DSB experiences a red shift to 1611 $cm^{-1}$ in DSB-$MoS_2$ spectra. Furthermore, the peak 3404 $cm^{-1}$ in the SB and DSB spectra undergoes a blue shift to 3435 $cm^{-1}$ in the FTIR spectra of DSB-$MoS_2$. The FTIR studies confirm the successful *in-situ* growth of $MoS_2$ on DSB qualitatively and further quantitatively measured using XPS and EDX studies.

XPS studies of DSB and DSB-$MoS_2$ were carried out to investigate the changes in surface functionalities and understand the mechanism of the *in-situ* growth of $MoS_2$ on the surface of DSB. ***Figure 4.2*(c)** represents the XPS survey of DSB-$MoS_2$ with peaks at 532.08 eV, 285.08 eV, 232.08 eV, and 162.08 eV representing *O1s*, C1s, *Mo3d*, and *S2p* bonds respectively. The broad spectrum of *Mo3d* (***Figure 4.2*(d))** has prominent peaks at 235.8 eV, 232.4 eV, 229.18 eV, 228.5 eV, and 224.8 eV that correspond to Mo-O-C bonds, $Mo3d_{3/2}$ signifying Mo (IV) oxidation state of *2H*-$MoS_2$, $Mo3d_{5/2}$, Mo-S bonds and Mo based sulphide respectively [392–395]. The high-resolution spectrum of *O1s* (***Figure 4.2*(e)**) has a major peak at 532.08 eV, which on deconvolution represents Mo-O (530.7 eV) and C=O (532.2 eV) [396]. The broad spectrum of *C1s* (***Figure 4.2*(f)**) has a prominent peak at 284.68 eV, which, upon deconvolution, is subdivided into three peaks at a binding energy of 284.6 eV, 286.2 eV and 286.6 eV that represent C-C, C-O, and C-O-C bond respectively [397–399].

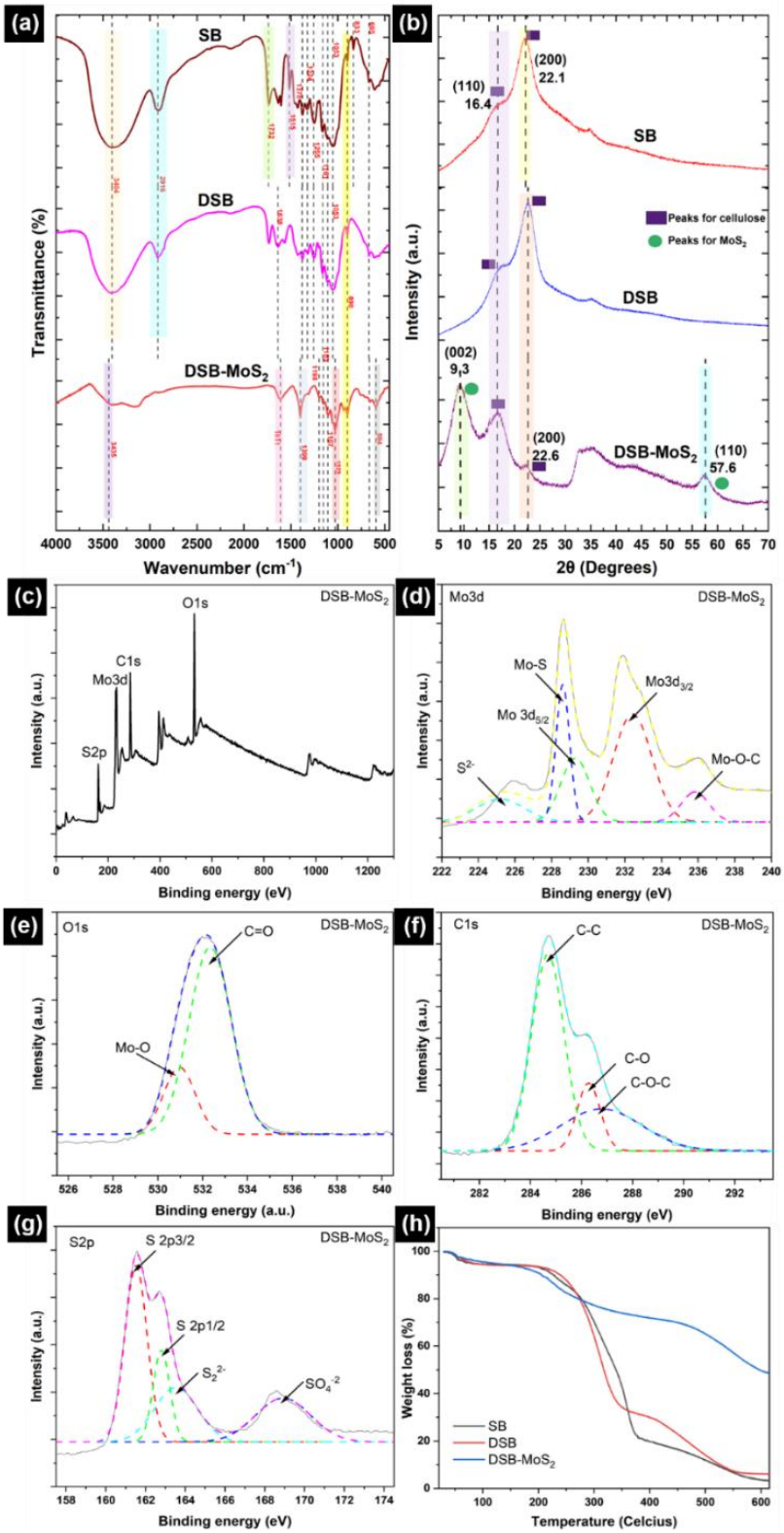


***Figure 4.2*** *Illustrate (a) FTIR spectra, (b) XRD pattern of SB, DSB, and DSB-$MoS_2$, (c) XPS survey of DSB-$MoS_2$, a broad spectrum of (d) C1s, (e) O1s, (f) Mo3d, (g) S2p, and (h) TGA signals of SB, DSB, and DSB-$MoS_2$.*

The XPS spectra of *S2p* (***Figure 4.2*(g)**) have peaks at a binding energy of 168.8 eV, 163.2 eV, 162.8 eV, and 161.53 eV that correspond to $SO_4^{2-}$, $S_2^{2-}$, $S2p_{1/2,}$ and $S2p_{3/2}$ [400–403]. The ***Figure 4.3*(a)** represents the XPS survey of DSB with peaks at 533.08 eV and 285.08 eV (binding energy) representing *O1s* and *C1s* bonds, respectively. The broad spectrum of *C1s* (***Figure 4.3*(b)**) has a major peak at 284.68 eV, which upon deconvolution represents two peaks, 285.9 eV and 284.5 eV, representing C-O and O=C-O bonds, respectively [404]. The broad spectrum of *O1s* (***Figure 4.3*(c)**) has a major peak at 532.6 eV that depicts the C-O bond [405]. No peaks were observed in the XPS of DSB for Mo and S, as shown in ***Figure 4.3*(d-e)**, with only noise observed in the spectra. The elemental composition of DSB-$MoS_2$ **(*Table 4.1*)** shows a high content of Mo ~9.49 and S ~15.77 atomic %, which were in-line with EDX spectroscopy studies. Mo-S, Mo-O-C, and Mo-O bonded interactions from the XPS spectra indicate the successful *in-situ* growth of $MoS_2$ nanosheets on the cellulose backbone structure present in DSB. Therefore, it could be confirmed that the presence of charge-based electrostatic interactions between the hydroxyl groups in cellulose backbone and molybdate salts helped in both adhesion and growth of $MoS_2$ nanosheets, which further self-assembled into nanoflower-like structures, as shown mechanistically in ***Figure 4.1***.

The thermogravimetric curves of SB, DSB, and DSB-$MoS_2$ are illustrated in ***Figure 4.2*(h),** and the thermogravimetric parameters are calculated as shown in ***Table 4.2***. TGA thermograms of SB, DSB, and DSB-$MoS_2$, the first stage of weight loss ~ 5.53 %, 5.54 %, and 4.61 %, respectively, are observed in the temperature range of 30-105 °C, which is due to the evaporation of water or moisture present. The onset thermal degradation temperature ($T_{onset}$), i.e., 10 % weight loss, was observed at 226 °C for SB, 238 °C for DSB, and 204 °C for DSB-$MoS_2$. The thermograms of SB and DSB show

single-stage degradation behaviour with $T_{max}$ of ~379 °C and 360 °C, respectively, with % degradation at $T_{max}$ ~78.74 % and 67.06 %. Interestingly, DSB-$MoS_2$ demonstrated high thermal stability with two stages of decomposition, the first stage from 216 °C - 423 °C (% degradation at $T_{max}$ = 28.96 %) and the second stage from 448 °C - 600 °C (% degradation at $T_{max}$ = 51.32 %). The residual weight percentage of SB, DSB, and DSB-$MoS_2$ at 600 °C was 3.68 %, 6.19 %, and 49.53 % respectively. DSB-$MoS_2$ exhibited higher thermal stability with increased charred residue than SB/DSB, mainly due to the presence of thermally stable $MoS_2$ nanosheets, as reported in previous studies [152].

### 4.2.2 Structural investigation of DSB and DSB-$MoS_2$

XRD diffractogram (***Figure 4.2*(b)**) studies were performed to understand the effect of delignification on the crystal structure of SB and *in-situ* growth of $MoS_2$ nanosheets on DSB *via* hydrothermal treatment. The XRD diffraction pattern of SB shows two distinct peaks at 2θ ~16.4° and 22.1°, which corresponds to the (110) and (200) crystal planes of cellulose, respectively [406]. After the delignification step, a peak shift in the XRD pattern of DSB is observed from 2θ = 22.1° to 22.6°. After the hydrothermal treatment, the XRD pattern of DSB-$MoS_2$ shows distinct peaks at 2θ = 9.3°, 16.4°, 22.6° and 57.6°, which represent the lattice planes (002), (110), (200), and (110) corresponding to both cellulose and $MoS_2$, respectively [407,408]. The presence of $MoS_2$ in the hydrothermally processed composites was confirmed from the peaks at 2θ = 9.3° and 57.6°, which correspond to the hexagonal phase of $MoS_2$ [407,408].

The crystallite size and *d*-spacing of SB, DSB, and DSB-$MoS_2$ were calculated and reported in ***Table 4.3*** The *in-situ* growth of nanosheets in the cellulose inter-layers of the DSB-$MoS_2$ resulted in the decrease in the *d*-spacing corresponding to planes of

2θ = 22.6°. The crystal lattice peaks and the change in crystal structure confirms the formation and *in-situ* growth of $MoS_2$ nanosheets, followed by self-assembly to form nano-flower-like structures as evaluated from morphological analysis, discussed in a subsequent section.

***Table 4.1*** *Represents the elemental composition of DSB and DSB-$MoS_2$ determined through XPS spectroscopic studies.*

| Sample | Carbon | Oxygen | Sulphur | Molybdenum |
|---|---|---|---|---|
| DSB (atomic %) | 78.2 | 20.75 | - | - |
| DSB-$MoS_2$ (atomic %) | 47.85 | 26.89 | 15.77 | 9.49 |

***Table 4.2*** *Thermogravimetric parameters of SB, DSB, and DSB-$MoS_2$*

| Sample Name | $T_{onset}$ | $T_{max}$ (°C) | $T_{max}$ (% degradation) | Char (%) |
|---|---|---|---|---|
| SB | 226 °C | 379 °C | 78.74 % | 3.68 % |
| DSB | 238 °C | 360 °C | 67.06 % | 6.19 % |
| DSB-$MoS_2$ | 204 °C | 216 °C – 423 °C | 28.96 % | 49.53 % |
| | | 448 °C – 600 °C | 51.32 % | |

***Table 4.3*** *Crystal structure properties of SB, DSB, and DSB-$MoS_2$ determined through XRD.*

| Samples | 2θ (°) | Crystallite size (nm) | *d*-spacing (nm) |
|---|---|---|---|
| SB | 16.4 | 0.0405 | 0.5398 |
| | 22.1 | 0.0160 | 0.4017 |
| DSB | 16.4 | 0.0553 | 0.5398 |
| | 22.6 | 0.0192 | 0.3929 |
| DSB-$MoS_2$ | 16.4 | 0.0407 | 0.5398 |
| | 22.6 | 0.0660 | 0.3929 |

### 4.2.3 Raman spectroscopy of DSB-$MoS_2$

Raman spectroscopy was performed to examine the molecular fingerprint of layered material. ***Figure 4.3*****(f)** shows four distinct peaks at 280 $cm^{-1}$, 362 $cm^{-1}$, 397 $cm^{-1}$ and 442 $cm^{-1}$ in the DSB-$MoS_2$. The 280 $cm^{-1}$ peaks observed in Raman spectroscopy

are associated with the $E_{1g}$ mode [409] and *2H*-$MoS_2$ phase [410], but the notable 362 $cm^{-1}$ peak is related to the $E_{2g}$ phonon vibration mode [411]. This mode entails the vertical movement caused by the lateral oscillation of two sulphur atoms and molybdenum atoms in opposing orientations inside the same plane. Furthermore, a prominent peak at 397 $cm^{-1}$ is attributed to the out-of-plane vibrational modes of $A^1g$, whereby the motion of two sulphur atoms is perpendicular to the plane [412]. Peaks within the 440-460 $cm^{-1}$ range indicate the existence of sulphur vacancies [413]. $E_{2g}$ and $A_{1g}$ modes have frequencies of 362 $cm^{-1}$ and 397 $cm^{-1}$, respectively. The 35 $cm^{-1}$ wavenumber difference between these modes is a reliable measure of the quantity of layers present in $MoS_2$.The measured discrepancy of 35 $cm^{-1}$ indicates the presence of multi-layered $MoS_2$ in this investigation [414,415].

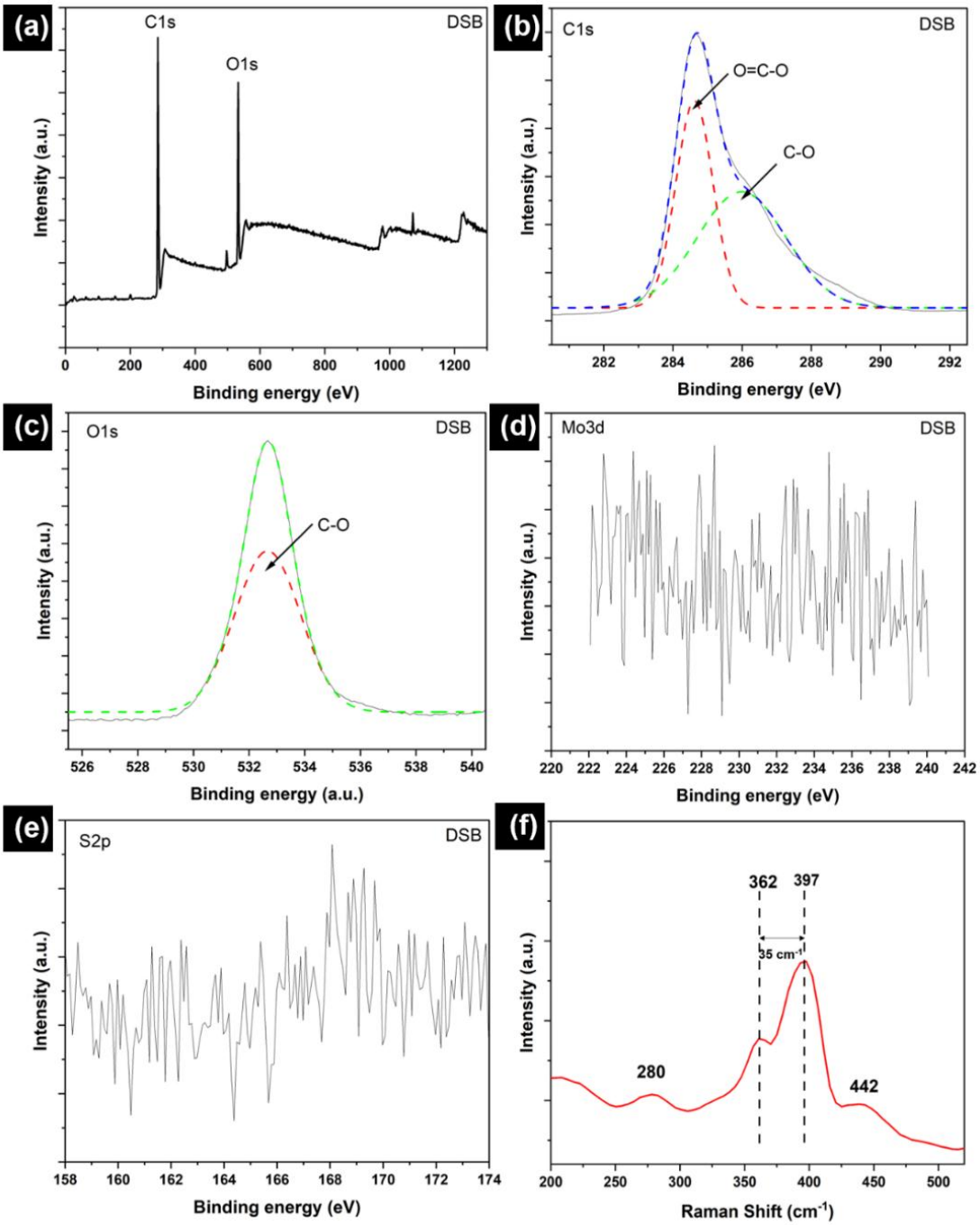


***Figure 4.3*** *XPS survey (a) broad spectrum of DSB, with a small scan section of (b) C1s, (c) O1s (d) S2p, (e) Mo3d of DSB, and (f) Raman spectroscopy of DSB-$MoS_2$.*

### 4.2.4 Morphological properties of DSB and DSB-$MoS_2$

The changes in the morphological properties of DSB on *in-situ* growth of $MoS_2$ nanoflowers are demonstrated in SEM micrographs, as shown in ***Figure 4.4***. ***Figure 4.4*****(a)** presents the rough, vertically aligned, and porous structure of DSB. A high-

resolution micrograph of DSB (***Figure 4.4*(b-d)**) represents a microporous honeycomb-like structure with a net-like entangled structure of cellulose fibres and the presence of a porous structure originating from the delignification process [416]. The rough and porous structure of DSB improves the adsorption of pollutant dye by providing a larger surface area for contact, facilitating mass transfer, improving accessibility to adsorption sites, and promoting concentration gradients for efficient adsorption. The growth of $MoS_2$ on the surface of vertically aligned DSB microfibers is shown in ***Figure 4.4*(e)-(h).** ***Figure 4.4*(e) & (f)** demonstrates the low-magnification micrograph of DSB-$MoS_2$ composite with porous and aligned cellulose micro-channels on which $MoS_2$ nanoparticles are uniformly distributed. At higher magnification (***Figure 4.4*(g)**, the presence of $MoS_2$ in spherical nanoflowers can be observed. The high-resolution image of $MoS_2$ nanoflowers, as shown in ***Figure 4.4*(h),** represents the aggregation of multiple spherical $MoS_2$ nanosheets.

The average pore size distribution of DSB was 29.14 µm (as shown in ***Figure 4.5*(a)**). At high temperatures, $MoS_2$ grows as nanosheets, which assemble, forming spherical nanoflower clusters with an average size distribution of ~377.13 nm (***Figure 4.5*(b))**. The elemental composition of DSB was confirmed by EDS in ***Figure 4.5*(c)** in terms of their atomic and weight %, which is in line with XPS studies. ***Figure 4.5*(d)** illustrates the elemental distribution of DSB-$MoS_2$. Additionally, individual maps for carbon (C) **(*Figure 4.5*(e))**, oxygen (O) **(*Figure 4.5*(f)),** molybdenum (Mo) **(*Figure 4.5*(g)),** and sulphur (S) **(*Figure 4.5*(h))** are provided.

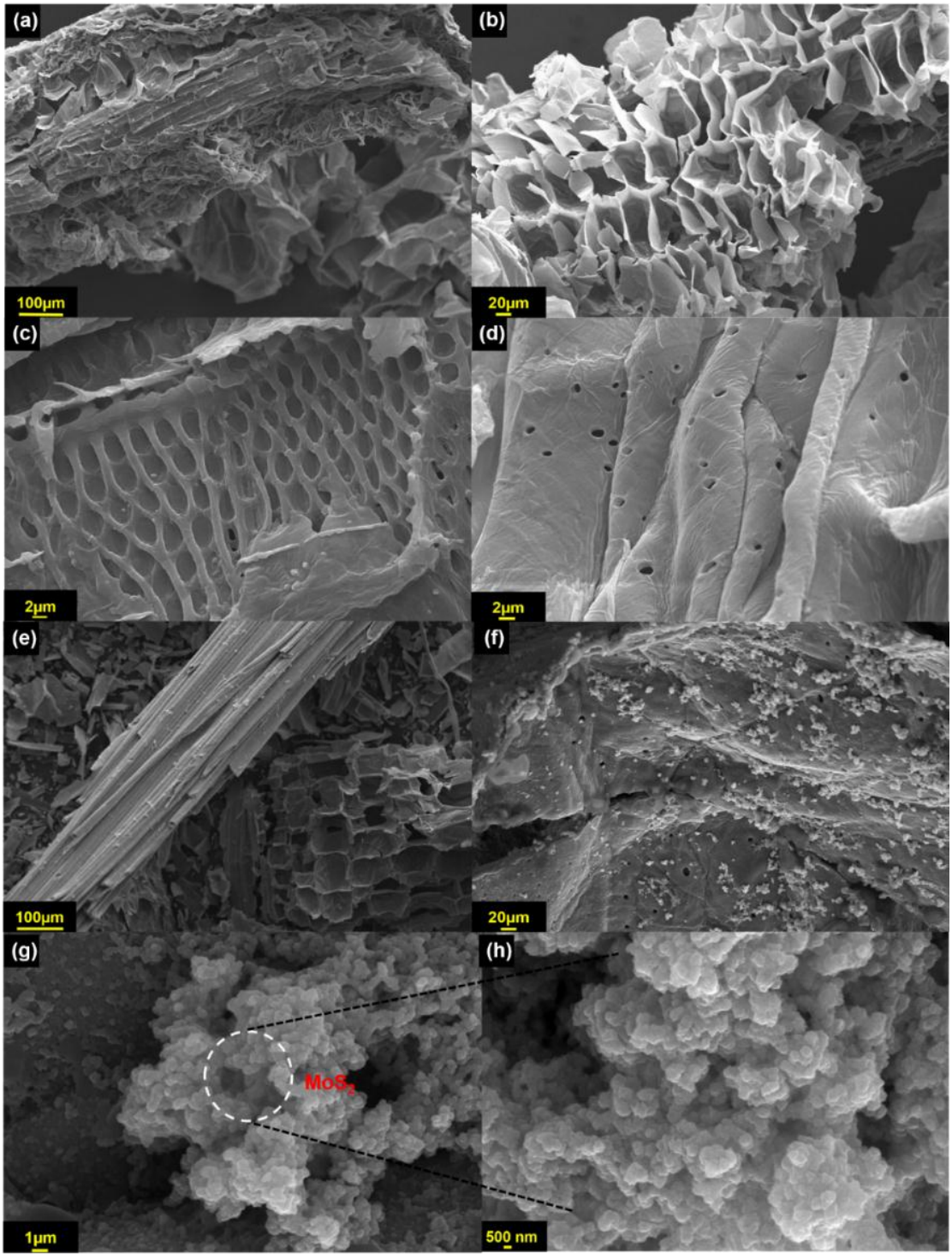


***Figure 4.4*** *SEM micrograph of developed composites (a) depicts micrograph of DSB at low resolution, (b), (c), (d) SEM-images of DSB at higher magnification, and (e) low-resolution micrograph of DSB-$MoS_2$, (f) high-resolution micrograph DSB-$MoS_2$ with of vertically aligned cellulose inter-layers (g) uniformly distributed $MoS_2$ nanosheets grown on DSB, (h) high-resolution micrograph of self-assembled $MoS_2$ nanoflowers.*

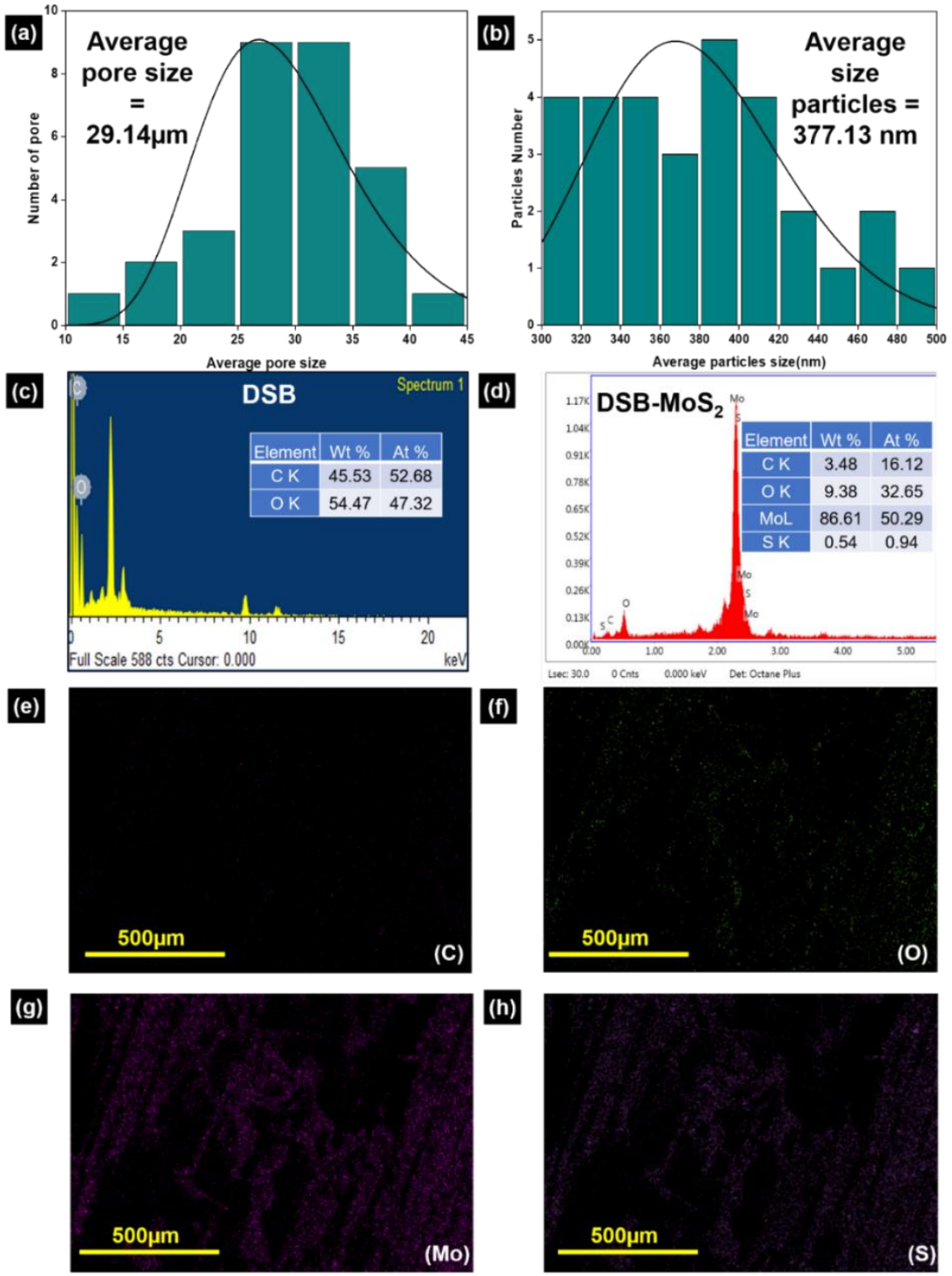


***Figure 4.5*** *(a) Average pore size distribution of DSB, (b) particle size distribution of $MoS_2$ nanoflowers, EDS spectrograph of (c) DSB, (d) DSB-$MoS_2$, elemental mapping of (e) Carbon (f) Oxygen (g) Molybdenum and (h) Sulphur.*

### 4.2.5 Adsorption of MB with DSB

Adsorption of MB with DSB ***Figure 4.6*****(a)** shows the percentage of MB adsorption using DSB at various dye concentrations. The % MB adsorption was observed to vary from 94 % to 68 % at dye concentrations ranging from 100 to 700 mg/L, with a maximum adsorption capacity of 80.2 mg/g. At a concentration of 100 mg/L, the maximum adsorption was 94 %. The adsorption percentages decreased as the MB concentration increased to 200, 300, and 500 mg/L to 90.5 %, 87.45 %, and 84.3 % respectively. At a concentration of 700 mg/L, the lowest adsorption percentage (68.7 %) was observed. Adsorption experiments of MB were conducted under a light source using DSB, yielding adsorption percentages of 95.4 %, 92.4 %, 91.5 %, 87.0 %, and 72.1 % for MB concentrations of 100, 200, 300, 500, and 700 mg/L, respectively. The overall adsorption capacity of DSB increased from 80 to 84 mg/g when the adsorption experiment was performed under light exposure. These results suggest that there was only a marginal increase in the adsorption percentage due to a slight increase in the temperature of MB solution upon exposure to light (***Table 4.4***). The presence of abundantly available hydroxyl groups in DSB may be responsible for the adsorption behaviour of MB dye through charge-based electrostatic interactions. These groups become saturated as the dye concentration increases, lowering the adsorption percentage. The decrease in MB adsorption percentage with increasing concentration from 100 to 700 mg/L could be attributed to a lack of active sites or the system reaching saturation and equilibrium [417].

#### 4.2.5.1 Effect of pH and temperature

The pH influences dye adsorption behaviour by altering the adsorbents' surface charge, the extent of ionization of available functional groups, and the adsorbate

speciation. The adsorption percentage of MB on the surface of DSB shows improvement with an increase in pH from 3 to 9 (***Figure 4.6*(b)**). The highest adsorption of MB was achieved at pH 11 (95 %), and the lowest was at pH 3 (81 %). The *pKa* value of MB is approximately 3.14, indicating its acidic characteristics below pH 3.14, where it carries a positive charge [418]. The reduction in percentage adsorption of MB at pH 3 and 5 primarily results from the high concentration of $H^+$ ions and the overall positive charge of MB. These factors led to electrostatic repulsion between the $H^+$ ions and positive charge of MB, causing a decreased adsorption percentage. Additionally, as pH of the MB solution increased from 5 to11, the concentration of $OH^-$ ions on the surface of DSB showed a noticeable improvement. This increase in $OH^-$ ions is responsible for the enhanced adsorption capacity, improving the percentage of MB adsorbed from 81 % to 95 %. The impact of temperature on MB adsorption percentage using DSB was examined over a 25 °C to 45 °C temperature range. The results are shown in ***Figure 4.6*(c)** suggested that with the rise in temperature from 25°C to 45 °C, the percentage of MB adsorption escalated from 81.66 % to 95.1 %. The adsorption percentage of MB were 81.6 %, 83 %, 85.2 %, 91.6 %, and 95.18 % at 25 °C, 30 °C, 35 °C, 40 °C, and 45 °C respectively. An increase in MB solution temperature increases dye molecules' kinetic energy. It accelerates the rate of MB diffusion to the surface and within the porous structure of DSB, consequently increasing the percentage of MB adsorption [419].

### 4.2.5.2 Adsorption kinetics and isotherm

Adsorption kinetics studies are essential to comprehend the mechanism of adsorption processes among adsorbate (MB) and adsorbent (DSB). The experimental data were linearly fitted with PFO and PSO models to study the adsorption kinetics, shown in ***Figure 4.6*(d)** and ***Figure 4.6*(e)**.

According to the correlation coefficient value (R2), Qe experimental, and Qe calculated (presented in ***Table 4.5*****),** it was evident that the PSO kinetic model exhibited the best fit to the experimental data. The R2 values obtained for the PSO kinetic model at various concentrations of MB were consistently close to 0.99. This suggests that the adsorption of MB on DSB is primarily influenced by the adsorption capacity of DSB rather than the concentration of the dye [420]. Additionally, these results confirm that the adsorption of MB on DSB is predominantly controlled by chemisorption, which originates from charge-based interactions, and the adsorption rate is determined by the availability of binding sites on DSB [421].The fitted Freundlich and Langmuir isotherms are shown in ***Figure 4.6*****(f)** and ***Figure 4.6*****(g)**, respectively, with the corresponding parameters listed in ***Table 4.6.*** The $R^2$ values obtained for the linearly fitted experimental data using the Freundlich and Langmuir isotherms were 0.96 and 0.99, respectively. The following results suggest that the data collected from experiments closely aligns with the Langmuir isotherm, indicating that a monolayer of DSB controls the adsorption process [422]. The maximum monolayer capacity of the Langmuir isotherm ($Q_o$ = 93.4 mg/g) corresponds closely to the experimental data, and the adsorption rate constant ($b$) is 0.029.

### 4.2.5.3 Adsorption thermodynamics

The thermodynamic studies for the adsorption of MB onto the monolayer surface of DSB were performed to evaluate the exothermic or endothermic behaviour and to calculate the thermodynamic parameters such as entropy ($\Delta S^o$), enthalpy ($\Delta H^o$), and Gibb's free energy ($\Delta G^o$) (***Table 4.7)***. The experiment was performed at five different (25-45 $^0$ C) temperatures for 200 mg/L MB concentration and 300 minutes of contact time. The plot between $lnk_c$ and $1/T$ was used to calculate the values of $\Delta S^o$

(from intercept) and $\Delta H^0$ (from the slope), as shown in ***Figure 4.6*(h).** In this study, the range of $\Delta G^0$ values observed was between -0.075 to -2.44 kJ/mol across the investigated temperature range. The $\Delta G^0$ value decreases as the temperature decreases, indicating that a lower amount of energy is needed for the adsorption of MB on the DSB [422]. The negative sign associated with $\Delta G^0$ signifies that the adsorption process is spontaneous and favourable. The value of the $\Delta H^\circ$ was 32.66 kJ/mol, and the positive sign indicated the endothermic behaviour of the process, and the positive value of $\Delta S^\circ$ (109.82 J/mol) indicates the randomness in the adsorption behaviour at the monolayer of the DSB.

***Table 4.4*** *Comparison of adsorption percentage of MB using DSB in light and dark conditions.*

| Concentration (mg/L) | (%) Adsorption (without light) | % Adsorption (light) | Change in adsorption (%) |
|---|---|---|---|
| 100 | 94 | 95.4 | 1.4 |
| 200 | 90.5 | 92.4 | 1.9 |
| 300 | 87.45 | 91.5 | 4.05 |
| 500 | 84.3 | 87 | 2.7 |
| 700 | 68.7 | 72.1 | 3.4 |

***Table 4.5*** *PFO and PSO kinetic parameters for the adsorption of MB onto DSB.*

| Concentration (mg/L) | PFO kinetic | | PSO kinetic | |
|---|---|---|---|---|
| | $K_1$ | $R^2$ | $K_2$ | $R^2$ |
| 100 | 0.0058 | 0.87 | 0.013449 | 0.99 |
| 200 | 0.013 | 0.86 | 0.007181 | 0.99 |
| 300 | 0.00059 | 0.64 | 0.013101 | 0.99 |
| 500 | 0.007 | 0.74 | 0.000888 | 0.99 |
| 700 | 0.0102 | 0.85 | 0.00385 | 0.99 |

***Table 4.6*** *Details of the adsorption isotherm parameters for DSB.*

| **Langmuir isotherm** | | | **Freundlich isotherm** | | |
|---|---|---|---|---|---|
| $R^2$ | $B$ | $Q_0$ | $R^2$ | $K_F$ | $1/n$ |
| 0.99 | 0.02939 | 93.45794 | 0.96 | 2.2426 | 0.46 |

***Table 4.7*** *Adsorption thermodynamic parameter for DSB*

| **Temperature** | $\Delta G^o$ | $\Delta S^o$ | $\Delta H^o$ |
|---|---|---|---|
| 298.13 | - 0.0758 | 0.109 kJ/mol | 32.66 kJ/mol |
| 303.13 | -0.7398 | | |
| 308.13 | -1.1935 | | |
| 313.13 | -1.5113 | | |
| 318.13 | -2.4428 | | |

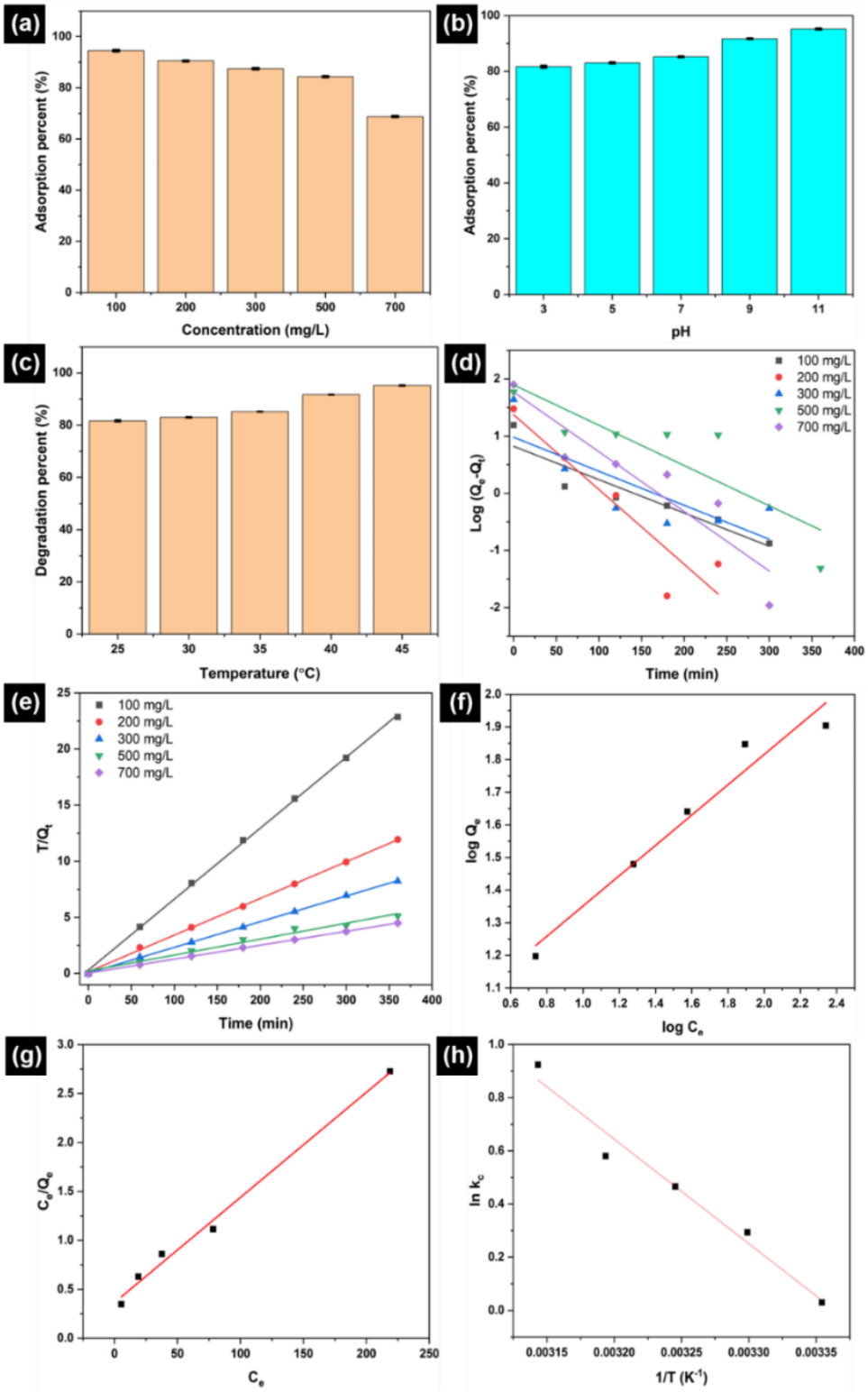


***Figure 4.6*** *Adsorption percentage of MB using DSB as adsorbent at (a) different dye concentrations, (b) variations of pH and (c) temperature, adsorption kinetics and isotherm studied using (d) linear fitting of pseudo-first-order (PFO) kinetic model, (e) pseudo-second-order (PSO) kinetic model, linear fitting of isotherms (f) Freundlich isotherm, (g) Langmuir isotherm and (h) adsorption thermodynamic.*

### 4.2.6 Photodegradation of MB using DSB-$MoS_2$

The degradation of MB was studied under two conditions: white light exposure and complete darkness ***Figure 4.7*****(a)**. This study used six different MB concentrations (100, 200, 300, 500, 700, and 1000 mg/L) in a 50 mL dye solution with 0.2 g of DSB-$MoS_2$. The photodegradation percentage of MB was found to be 99 % at concentrations of 100, 200, and 300 mg/L. However, the time required to achieve 99 % degradation varied depending on the concentration range. The maximum achieved degradation percentages for concentrations of 500 and 700 mg/L were 96.5 % and approximately 88.8 %, respectively. After 360 minutes of contact time, the MB concentration of 1000 mg/L had the lowest degradation percentage, achieving merely 63.4 %.

The photodegradation carried out under dark conditions shows the highest degradation percentages of 98 % for 100 mg/L MB concentration, approximately 86 % for 200 mg/L, 79 % for 300 mg/L, 75 % for 500 mg/L, 64 % for 700 mg/L, and 45.72 % for 1000 mg/L. However, the time required to achieve these photodegradation levels varied for each MB concentration was also studied. The reduction in MB degradation percentages at various concentrations without light can be attributed to adsorption only. This leads to 98 %, 86 %, 79 %, 75 %, 64 %, and 45.72 % adsorption for MB concentrations of 100, 200, 300, 500, 700, and 1000 mg/L, respectively. Nevertheless, MB performance improvements were noted when the light was exposed, with degradation enhancements of 1 %, 13 %, 20 %, 21.5 %, 24.8 %, and 17.68 % for 100, 200, 300, 500, 700, and 1000 mg/L, respectively. The decline in the degradation percentage of MB with an increased concentration range under both light and dark conditions can be attributed to the reduced catalytic activity of DSB-$MoS_2$ with increased adsorption of MB at high concentrations. This process hinders the exposure

of $MoS_2$ to light, thereby impeding the generation of –OH free radicals that are responsible for the photodegradation of MB. Similar observations were also found in the recent studies by Wu et al., Sadhanala et al., and Szkoda et al. [98], [99], [100] where MB degradation with $MoS_2$ under dark conditions was mainly attributed to the adsorption process. The decline in the degradation percentage of MB with an increased concentration range under both light and dark conditions can be attributed to the reduced catalytic activity of DSB-$MoS_2$ with increased adsorption of MB at high concentrations. This process hinders the exposure of $MoS_2$ to light, thereby impeding the generation of -OH free radicals that are responsible for the photodegradation of MB [423] [424].

#### 4.2.6.1 Effect of pH on photodegradation of MB

The pH affects the rate of photodegradation of dyes and the production of $H^+$ (protonation) or $OH^-$ (deprotonation) ions in a solution. Experiments were carried out under both light and dark conditions at various pH levels (pH 3, 5, 7, 9, and 11) to investigate the photodegradation following constant MB concentration of 200 mg/L, temperature at 30 °C and time of 6 hours, as shown in ***Figure 4.7*****(b)**. MB photodegradation was 81.6 % in the presence of light and 72.2 % in the absence of light under acidic conditions with a pH of 3. However, when the pH was raised to 5, the percentage degradation increased to 90.8 % in the presence of light and 79.8 % in the absence of light. Furthermore, when the pH elevated to 7, the percentage degradation of MB was almost 99 % under light, whereas 85.2 % degradation was achieved under completely dark conditions. Furthermore, when the pH increased was to 9 and 11 (alkaline condition), the percentage degradation of MB under light conditions was 99 %, whereas, under dark conditions, 90.4 and 93.8 % degradation was achieved,

respectively. The adsorption of $OH^-$ ions by DSB-$MoS_2$ at higher pH makes it negatively charged, resulting in an increased degradation percentage of MB when the pH of the solution shifts from highly acidic to highly alkaline conditions. As a result, the cationic MB dye easily adsorbs onto the DSB-$MoS_2$ surface, increasing the degradation percentage [424].

#### 4.2.6.2 Effect of temperature on photodegradation of MB

The effect of temperature on the degradation of MB was studied at temperatures ranging from 25 to 45 °C, under both light and dark conditions, at a fixed MB dye concentration of 200 mg/L and pH 7. ***Figure 4.7*(c)** shows that increasing the temperature of the solution from 25 to 45 °C under light conditions resulted in a minor improvement in the degradation percentage of MB, ranging from 97 % to 99 %. However, under complete dark conditions, the percentage of MB degradation reached 97 % as the solution temperature was raised to 45 °C. At high temperatures, dye molecules became more soluble and diffuse, making them easily accessible to interact with the photocatalytic reaction sites. An increase in the degradation of MB with an increase in the temperature defines the endothermic behaviour of the DSB-$MoS_2$. The improved interaction of dyes at the catalytic sites of DSB-$MoS_2$ with increased mobility at higher temperatures resulted in improved percentage degradation.

#### 4.2.6.3 Photodegradation kinetics

The degradation kinetics of MB were studied using the PFO (***Figure 4.7*(d))** and PSO (***Figure 4.7*(e))** kinetic model to understand the degradation rate and its mechanism, with parameters tabulated in ***Table 4.8***. Upon linear fitting of the experimental data using both models, it was observed that the correlation coefficients fell within the range of 0.92 - 1 for PSO. These results indicated a higher favourability

towards the PSO kinetic model for all the concentrations studied. Additionally, the calculated equilibrium adsorption capacity ($Q_o$) of 161.55 mg/g obtained from the PSO model closely matched the experimental $Q_e$ value of 158.74 mg/g. The improved charge-based interactions resulted in higher adsorption of MB followed by photodegradation on $MoS_2$, leading to chemisorption-like behaviour, which is in-line with the mechanism proposed in the PSO kinetic model.

#### 4.2.6.4 Continuous photodegradation behavior and recyclability studies of DSB-$MoS_2$

To evaluate the potential stability of the developed DSB-$MoS_2$ catalyst and its usage for the treatment of high-volume industrial-scale wastewater systems, a comprehensive study was carried out to investigate its continuous dye degradation capability and potential for reuse. The continuous dye degradation using DSB-$MoS_2$ (0.5 g dosage) was performed in a plug flow reactor under white light with an MB dye concentration of 200 mg/L maintained at 30 °C for five cycles, with each cycle continuing for 4 hours (***Figure 4.7*(g)**). The photodegradation percentage of MB (as shown in ***Figure 4.7*(f)**) in the first cycle was 99 %, which showed excellent catalytic properties of DSB-$MoS_2$. In the second cycle, the percentage degradation of MB was 96.8 %, which dropped to 83.4 % in the third cycle. This result suggests that the developed catalyst have good reusability upto 3 cycles. In the fourth and fifth cycles, the degradation percentage dropped to 67.3 % and 51.7 %, respectively. The decrease in the photodegradation percentage after the third cycle could have resulted from the leaching of the DSB-$MoS_2$ catalyst during the continuous flow of MB solution in the plug flow reactor over 30 hours of experiments and 1800 mL of dye solution. Similar findings were also observed in the recent literature [425–427]. SEM images of the catalyst after photodegradation show a uniform distribution of $MoS_2$ on the surface of

DSB, consistent with the SEM image before the experiment. The SEM analysis revealed the presence of $MoS_2$ nanoparticles on the surface of DSB-$MoS_2$, as depicted in ***Figure 4.8*****(a-d)**. Elemental mapping illustrated in ***Figure 4.8*****(e-g)** and EDS analysis shown in ***Figure 4.8*****(h)** confirmed the existence of Mo and S elements. From the discussion, it can be inferred that DSB-$MoS_2$ composite derived from renewable, sustainable agro-waste is an efficient, reusable, and stable catalyst which can be utilized for continuous treatment of contaminated wastewater at large scale and high volume.

### 4.2.7 Antibacterial properties of DSB-$MoS_2$

*S. aureus* and *E. coli* were used to evaluate the anti-bacterial properties and decontamination capabilities of DSB-$MoS_2$. The dispersion of DSB-$MoS_2$ was gently placed on freshly cultured *E. coli* and *S. aureus* plates using three different DSB-$MoS_2$ concentrations (0.1, 0.125, 0.15 wt. %). As illustrated in ***Figure 4.7*****(h)** and ***Figure 4.7*****(i),** the inhibition zones for the *E. coli* culture plate were 9, 12, and 12 mm, and that of the *S. aureus* culture plates were 7, 8, and 12 mm, respectively. The occurrence of the zone of inhibition on both cultured plates confirms the concentration-dependent antibacterial characteristics of the developed DSB-$MoS_2$ composites. The antibacterial properties of DSB-$MoS_2$ could be attributed to the inherent photocatalytic characteristics of $MoS_2$. When $MoS_2$ is directly exposed to light sources, ROS are produced, which aid in the destruction or inactivation of microorganisms *via* lysis of the cell membrane. The rupture of the membrane induces phospholipid extraction and damages the structural integrity of the lipid membrane of bacteria [152]. Therefore, the developed DSB-$MoS_2$ composites can be potentially used for simultaneous microbial decontamination and remediation of pollutant dyes, generally found in real wastewater samples, making them suitable for practical applications.

### 4.2.8 Mechanism of the photodegradation of MB

In the process of photocatalytic oxidation, visible light exposure to $MoS_2$ leads to photoexcitation, causing the generation of electron-hole pairs on the catalytic material's surface specifically, $e_{CB}^-$ arises from the conduction band (CB), and $h_{VB}^+$ originates from the valence band (VB) (equation 12). Oxygen vacancies on the catalyst surface function as electron traps, preventing the recombination of electron-hole pairs. The electron produced undergoes oxidation when it interacts with the oxygen molecules on the surface of $MoS_2$. This process leads to the production of an electron acceptor. The photogenerated hole can undergo rapid oxidation within the organic molecule or interact with water molecules or a hydroxyl ion to produce a hydroxyl radical ($OH^{\cdot}$) (equation 14 and equation 15). Lastly, the overall photodegradation reaction is carried out by the free radical ions $O_2^{\cdot -}$ and $OH^{\cdot}$ (equation 16-equation 18).

$$MoS_2 + h\upsilon\,(vis) \rightarrow MoS_2\,(e_{CB}^- + h_{VB}^+) \quad \text{(eq.12)}$$

$$MoS_2(e_{CB}^-) + O_2 \rightarrow MoS_2 + O_2^{\cdot -} \quad \text{(eq.13)}$$

$$MoS_2\,(h_{VB}^+) + H_2O \rightarrow MoS_2 + H^+ + OH^{\cdot} \quad \text{(eq.14)}$$

$$MoS_2\,(h_{VB}^+) + OH^- \rightarrow MoS_2 + OH^{\cdot} \quad \text{(eq.15)}$$

$$O_2^{\cdot -} + H_2O \rightarrow H^{\cdot}O_2 + OH^- \quad \text{(eq.16)}$$

$$H^{\cdot}O_2 + H_2O \rightarrow H_2O_2 + HO^{\cdot} \quad \text{(eq.17)}$$

$$HO^{\cdot} + MB \rightarrow CO_2 + H_2O \quad \text{(eq.18)}$$

Finally, when MB interacts with highly reactive hydroxyl radicals, it undergoes degradation with $CO_2$ and $H_2O$ generation.

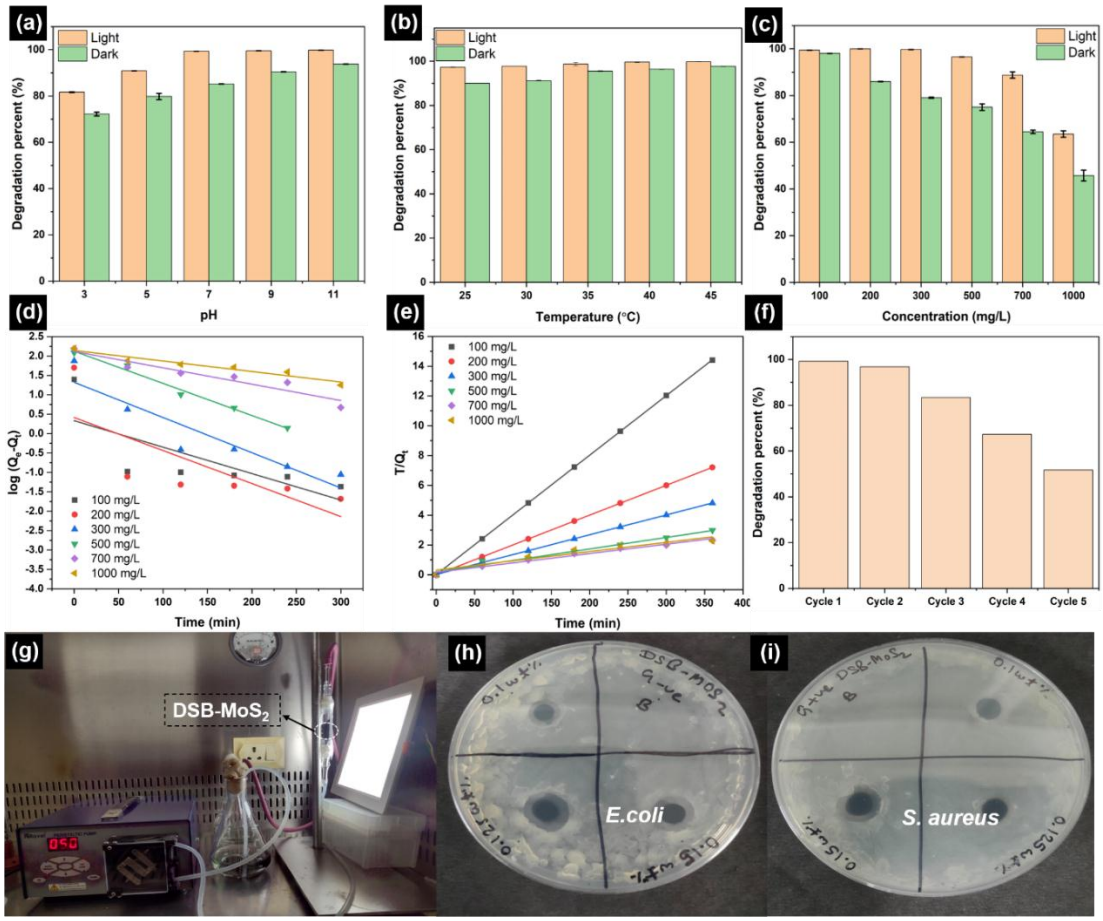


***Figure 4.7*** *Represent the percent photodegradation of MB using DSB-$MoS_2$ under dark and light conditions, (a) at different dye concentrations, (b) pH and (c) temperature, (d) linear fit of PFO kinetic model, (e) PSO kinetic model, (f) setup for the continuous degradation of MB under a white light source, (g) effect on percent photodegradation of MB during reusability of DSB-$MoS_2$, the antibacterial activity of DSB-$MoS_2$ (h) against E. coli and (i) S. aureus.*

***Table 4.8*** *PSO and PSO kinetic parameters for photodegradation of MB using DSB-$MoS_2$.*

| Concentration (mg/L) | PFO kinetic | | PSO kinetic | |
|---|---|---|---|---|
| | $K_1$ | $R^2$ | $K_2$ | $R^2$ |
| 100 | 0.00681 | 0.54 | 0.138685 | 1 |
| 200 | 0.0085 | 0.56 | 0.2384 | 1 |
| 300 | 0.00907 | 0.85 | 0.008514 | 0.99 |
| 500 | 0.00829 | 0.98 | 0.000311 | 0.97 |
| 700 | 0.00421 | 0.9 | 0.000235 | 0.98 |
| 1000 | 0.00271 | 0.93 | 0.00012 | 0.92 |

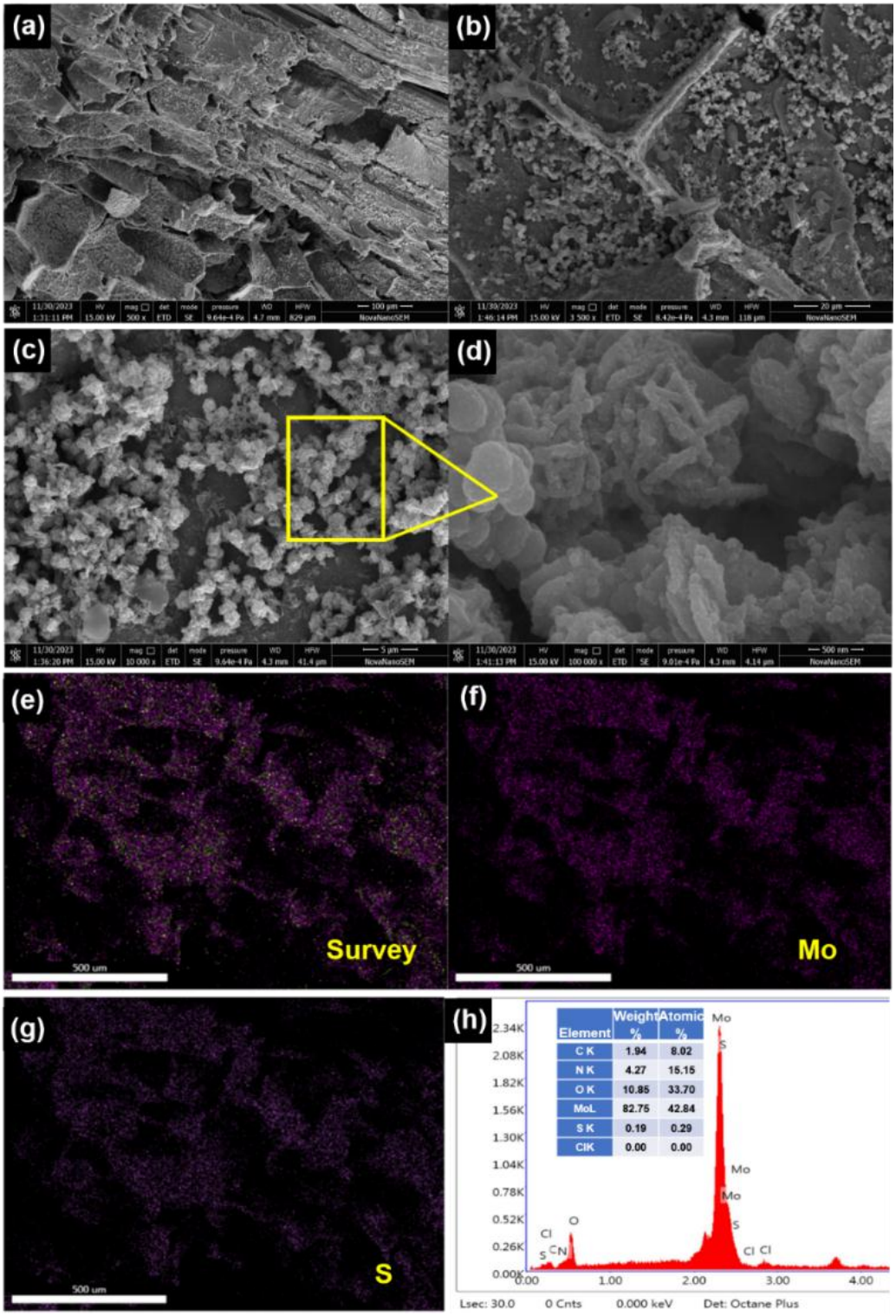


***Figure 4.8*** *Represent the SEM micrograph of (a) low-resolution micrograph of DSB-$MoS_2$-MB, (b-c) uniform distributed $MoS_2$ nanosheets grown on DSB, (d) high-resolution micrograph of self-assembled $MoS_2$ nanoflowers, elemental mapping of DSB-$MoS_2$-MB (e) survey of DSB-$MoS_2$-MB, (f) Molybdenum distribution on DSB-$MoS_2$-MB, (g) sulphur DSB-$MoS_2$-MB, and (h) EDS analysis of the DSB-$MoS_2$-MB.*

### 4.3 *In-situ* modification of DRH using $MoS_2$

Rice, one of the most consumed crops globally, generates large amounts of waste in the form of straws or husks during its processing, accumulating and posing harmful effects to the environment and aquatic life when disposed of conventionally (burning or landfilling) [428]. Therefore, the current investigation valorises the abundantly available, low-cost, lignocellulosic RH waste to remove chemo-biological contaminants from wastewater by simultaneous photodegradation of organic dyes and decontaminating pathogenic microbiota. Delignification of RH removes the aromatic lignin, exposing the cellulosic backbone's hydroxyl groups and providing sites for *in-situ* growth of $MoS_2$ nanosheets within the aligned cellulosic microstructure [429]. $MoS_2$ nanosheets localise randomly in the interlayers of cellulose microfibers self-assembling to form a nanoflower-like architecture, as schematically shown in ***Figure 4.9*** The performance of DRH-$MoS_2$ for adsorption and photodegradation of MG dye, a known carcinogenic agent mostly found in textile and food industry wastewater [430], was evaluated through mechanistic and kinetic studies. $MoS_2$, due to its catalytic properties, can absorb light in the visible range and generate free radicals that can potentially degrade organic contaminants such as dyes. The degradation efficiency of MG was evaluated under various temperatures, pH, and concentrations for dye adsorption and photodegradation. ROS generation by DRH-$MoS_2$ can also inflict damage to pathogenic microbes by cell lysis, which was evaluated through antibacterial studies. The improved MG removal efficiency and recyclability of DRH-$MoS_2$ during continuous degradation in plug-flow reactors show potential for industrially scalable and sustainable wastewater purification technologies derived from agro-biomass residues.

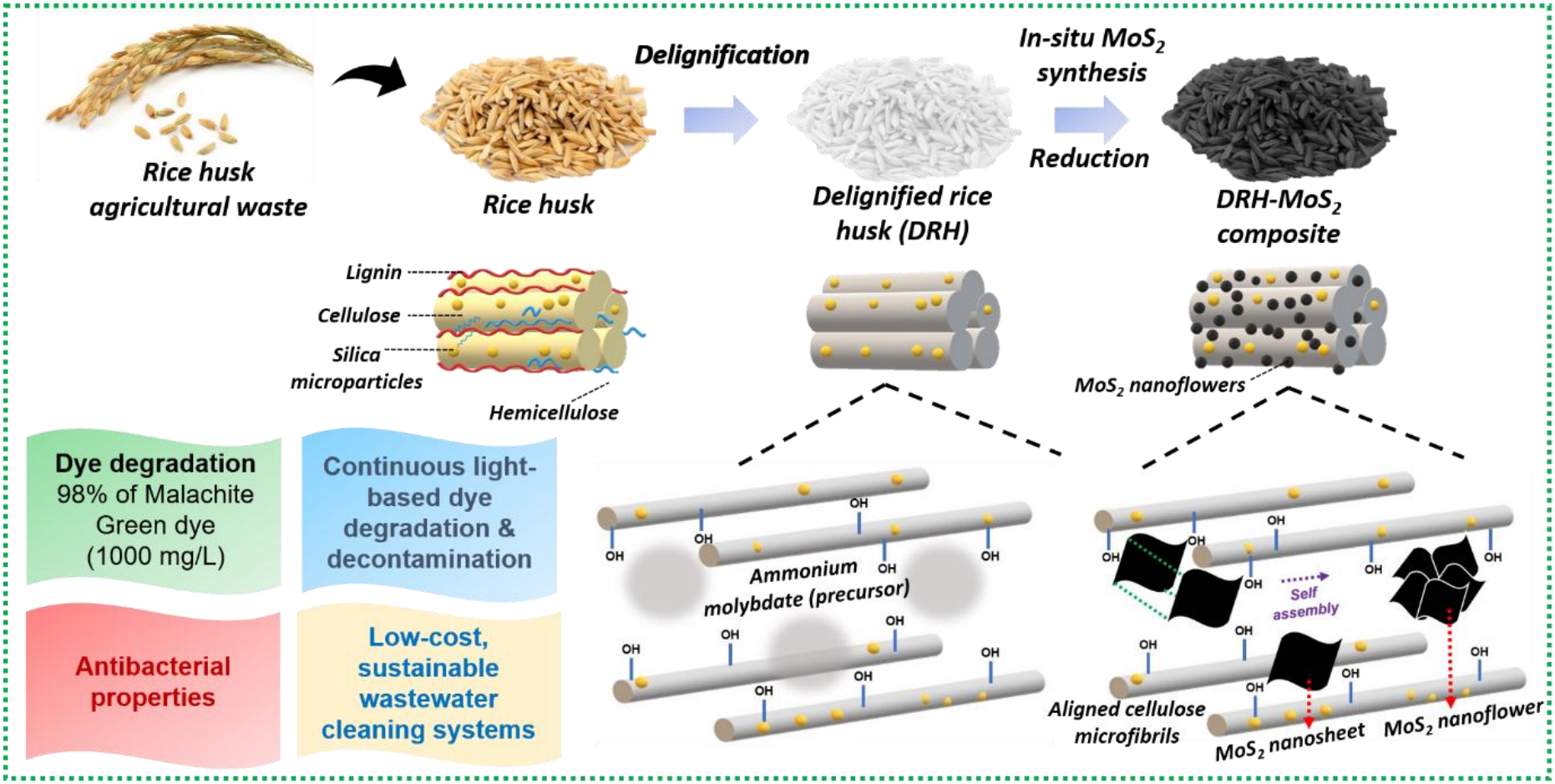


***Figure 4.9*** *Schematic for chemical modification of RH through strategic delignification followed by in-situ growth of $MoS_2$ nanosheets, which undergoes self-assembly to form $MoS_2$ nanoflowers with capabilities for the simultaneous dye adsorption, degradation, and microbial decontamination.*

### 4.3.1 Physicochemical and functional properties of DRH and DRH-$MoS_2$

The ATR-FTIR spectroscopy was used to determine functional groups in RH and DRH and confirm *the in-situ* growth of $MoS_2$ nanosheets in DRH-$MoS_2$ samples (***Figure 4.10*(a))**. The availability of IR peaks at 796 $cm^{-1}$, 1066 $cm^{-1}$, 1632 $cm^{-1,}$ and 3425 $cm^{-1}$ in RH, DRH, and DRH-$MoS_2$ samples correspond to Si-O bond, asymmetric Si−O−Si stretching vibrations, C=O stretching vibration of the carbonyl group in aldehyde and ketones, and bending vibration of -OH respectively. IR spectra at 2896 $cm^{-1}$ in DRH and DRH-$MoS_2$ correspond to the C-H stretching of cellulose achieved after the delignification of RH. The availability of peak at 1616 $cm^{-1}$ in RH and 1736 $cm^{-1}$ in DRH sample corresponds to the C=C bond of aromatic carbon of lignin and C=O stretching of acetyl groups arises due to the presence of hemicellulose respectively. Lastly, the IR peaks at 560 $cm^{-1}$, 664 $cm^{-1}$, 1107 $cm^{-1}$ and 1432 $cm^{-1}$ in the DRH-$MoS_2$ sample correspond to Mo-S [431], O-Mo-O stretching [432] S-S bond, and aliphatic C-H stretching respectively. The peaks at 560 $cm^{-1}$, 664 $cm^{-1}$, and 1107 $cm^{-1}$ confirm the *in-situ* growth of $MoS_2$ in the inter-layers of cellulose in DRH and are further confirmed by XPS and EDS studies, as discussed in the subsequent section.

XPS studies of DRH and DRH-$MoS_2$ were conducted to analyse the changes in the chemical linkages during the *in-situ* growth of $MoS_2$ on the DRH surface. The wide range XPS survey of DRH-$MoS_2$ **(*Figure 4.10*(c))** presents a peak for *O1s*, *C1s*, *Mo3d*, *S2p*, and *Si* groups at binding energy 531.1 eV, 283.6 eV, 231 eV, 153 eV, and 102.3 eV respectively. The narrow scan of *C1s* (***Figure 4.10*(d))** revealed three distinct subpeaks at 283.3 eV, 284.4 eV, and 285.6 eV, corresponding to the Mo-C bond, C=C, and Mo-O-C bond, respectively. The narrow O1s spectrum in ***Figure 4.10*(e)** was deconvoluted, revealing three subpeaks at binding energies of 531.1 eV, 532.7 eV, and

529.1 eV representing O-C=O bond, C-O bond and Mo-O bond respectively [433–435]. The narrow scanning of *Si* **(*Figure 4.10*(f))** presents a peak of 102.3 eV that can be further deconvoluted to $SiO_2$ (102.1 eV) and Si-O (102.9 eV) [436]. The peaks for *S2p* **(*Figure 4.10*(g))** were observed at 153.2 eV and 161.3 eV for $S2p_{1/2}$ and $S2p_{3/2}$, attributed to the binding energy of $S^{2-}$ [437]. Following the *in-situ* growth of $MoS_2$ on DRH, the emergence of Mo-C and Mo-O-C bonds indicates the formation of covalent bonds between $MoS_2$ and cellulose within DRH [438–440] The deconvoluted *Mo3d* peaks **(*Figure 4.10*(h))** show Mo-S bonds (233.9 eV), $Mo3d_{5/2}$ (228.9 eV) and $Mo3d_{3/2}$ (231 eV and 232.1 eV), signifying the Mo(IV) oxidation state of $MoS_2$ [437]. ***Figure 4.11*(a)** represents the XPS survey of DRH, with peaks at 533.08 eV, 285.08 eV, and 103.08 eV representing *O1s*, *C1s*, and Si bonds, respectively. In the high-resolution spectrum *C1s* in ***Figure 4.11*(b),** peaks at 284.4 eV, 286.02 eV, and 287.8 eV represent C-H, C-O-C, and C=O bonds, respectively, which represent the linkages from cellulose (DRH). In ***Figure 4.11*(c),** the peaks at 533.4 eV, 531.0 eV and 532.4 eV in the broad spectrum of *O1s* correspond to the C-OH bond, $SiO_2$ and C=O bond arises due to the presence of inherent silica in RH [441,442]. In ***Figure 4.11*(d),** narrow scanning of *Si* presents a peak at 103.2 eV that could be further deconvoluted to $SiO_2$ (103.8 eV) and Si-O-Si (103.1 eV) and Si-C (101.2 eV) [443,444], occurring due to silica embedded in aligned cellulose microfibrils. No peaks were observed in the XPS of DRH for the Mo and S, as shown in ***Figure 4.11*(e) and *Figure 4.11*(f)**, with only noise observed in the spectra. The in-depth analysis of XPS and FTIR spectroscopy suggests that molybdenum salts adsorbed onto hydroxyl groups in DRH through electrostatic interactions underwent successful reduction to form $MoS_2$ nanosheets.

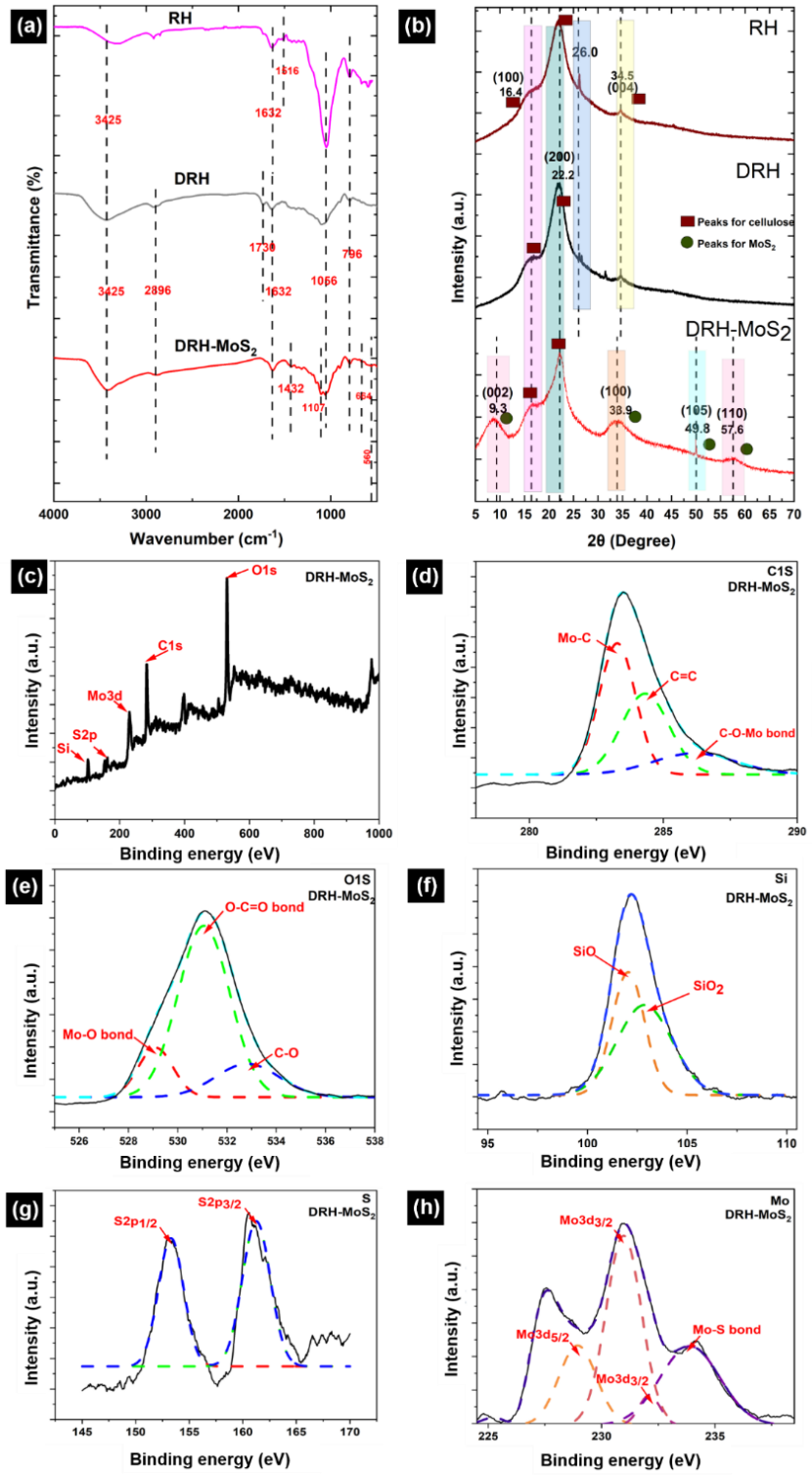


***Figure 4.10*** *Physicochemical, functional, and structural properties: (a) FTIR spectrum, (b) XRD spectrum of RH, DRH, and DRH-$MoS_2$, (c) XPS survey a broad spectrum of DRH-$MoS_2$, with small scan section of (d) C1s, (e) O1s, (f) Si2p, (g) S2p and (h) Mo3d of DRH-$MoS_2$.*

Moreover, it was observed that $MoS_2$ nanosheets dispersed uniformly in DRH underwent self-assembly to form nanoflower structures, which were governed by hydrogen bonds. The elemental composition of DRH and DRH-$MoS_2$ (***Table 4.9***) shows the presence of S ~3.36 and Mo~1.05 atomic %, which were absent in the DRH. Additionally, the energy band gap of DRH-$MoS_2$ was assessed through UV-DRS analysis. Tauc's plot revealed a determined band gap of 1.37 eV for DRH-$MoS_2$. The observed narrow band gap in DRH-$MoS_2$ further suggests the potential of these composites to serve as effective photocatalysts, particularly under visible light exposure [374].

***Table 4.9*** *Elemental composition of DRH and DRH-$MoS_2$ determined through XPS spectroscopic studies.*

| **Element** | **DRH-$MoS_2$ (Atomic (%)** | **DRH Atomic (%)** |
|---|---|---|
| *C* | 50.05 | 53.3 |
| *O* | 38.66 | 36.78 |
| *Si* | 6.89 | 9.9 |
| *S* | 3.36 | - |
| *Mo* | 1.05 | 0.02 |

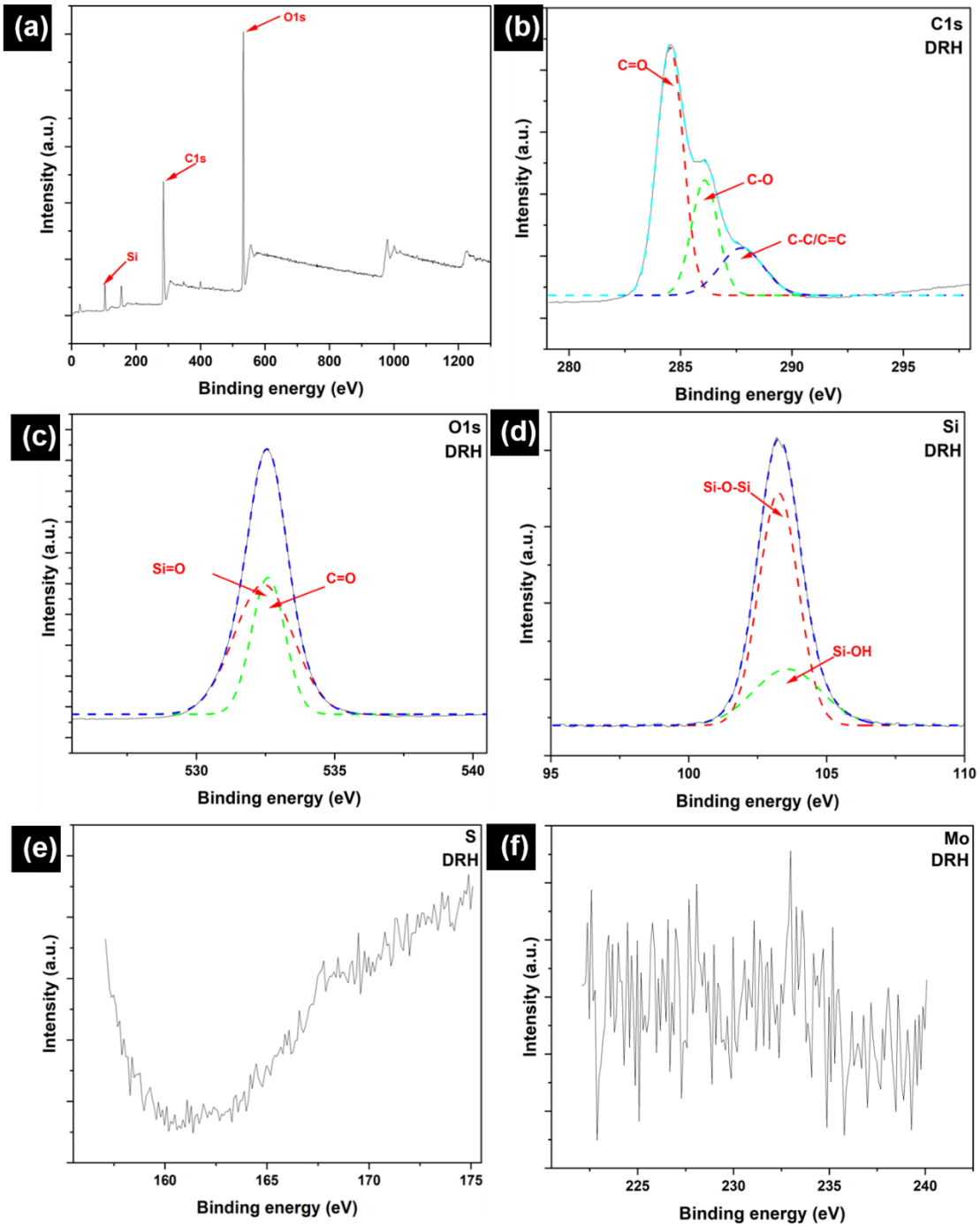


***Figure 4.11*** *XPS full scan spectra of DRH (a), broad scan spectra of (b) C1s, (c) O1s, (d) Si2p, (e) S2p and (f) Mo3d of DRH.*

### 4.3.2 Structural investigation of DRH and DRH-$MoS_2$

XRD diffractogram helps understand the influence of hydrothermal treatment on the *in-situ* growth of $MoS_2$ nanosheets on the cellulosic backbone in DRH. In the XRD diffractogram of RH, DRH and DRH-$MoS_2$, three distinct peaks were observed at 2θ = 16.4°, ~22.2° and 34.5° **(*Figure 4.11*(b)),** which corresponds to the (110), (200), and (004) crystal planes of cellulose I allomorphs, respectively. The sharp peak at 2θ = 26.0° in the DRH and RH samples was primarily due to silica's presence [445]. The diffraction pattern remained consistent throughout the cellulose extraction process. Still, there was a noticeable increase in peak intensities in DRH after delignification, resulting in higher crystallinity values for each sample. RH's crystallinity index (*C.I.*) was found to be 45.6 %, which, on delignification, improved to 51.3 % in DRH. However, after hydrothermal treatment, XRD spectra of DRH-$MoS_2$ show three new and distinct peaks at 2θ = 9.3°, 33.9°, 49.8° and 57.6° which represent lattice planes (002), (100), (105), and (110) respectively correspond to the hexagonal $MoS_2$ or *2H*-$MoS_2$ phases **(*Figure 4.11*(b))**. It was observed that after the *in-situ* growth of $MoS_2$ nanosheets, the crystallinity index (*C.I.*) of DRH-$MoS_2$ reduced to 30 % compared to the *C.I.* of DRH ~51.3 %. The reduction in *C.I.* for DRH-$MoS_2$ could be attributed to the hydrolysis, degradation and polymerisation of cellulose structure on prolonged reaction time and temperature during hydrothermal reaction [446]. Following hydrothermal treatment, the peaks of DRH-$MoS_2$ exhibit broadening, accompanied by a decrease in peak intensity, leading to a reduction in crystallinity [447]. Changes in the crystallite size and *d*-spacing were also observed in RH and DRH samples post-hydrothermal treatment **(*Table 4.10*)**.

***Table 4.10*** *Crystal structure properties of RH, DRH and DRH-$MoS_2$ determined through XRD.*

| Samples | *2θ (°)* | *C.I.* (%) | Crystallite size (nm) | *d*-spacing (nm) |
|---|---|---|---|---|
| RH | 16.4 | 45.63 | 0.039 | 0.532 |
| | 22.2 | | 0.023 | 0.404 |
| DRH | 16.4 | 51.30 | 0.04 | 0.537 |
| | 22.2 | | 0.027 | 0.401 |
| DRH-$MoS_2$ | 16.4 | 30 | 0.012 | 0.514 |
| | 22.2 | | 0.0190 | 0.401 |

### 4.3.3 Morphological properties of DRH and DRH-$MoS_2$

Morphological changes in DRH during *in-situ* growth of $MoS_2$ and their distribution were determined by SEM-EDXS analysis. As shown in ***Figure 4.12*****(a)**, DRH shows an aligned, porous, and rolled shape structure with regularly spaced silica microparticles. The surface of DRH was observed to have a protruded and rough appearance due to the presence of silica at the outer surface (***Figure 4.12*****(b)),** as also reported in earlier studies [448]. The low magnification SEM micrograph of DRH-$MoS_2$ shows the distribution of $MoS_2$ on DRH, as shown in ***Figure 4.12*****(c).** The formation of $MoS_2$ nanoflower structures ***Figure 4.12*****(d-f)** results from the self-assembly of $MoS_2$ nanosheets formed during *in-situ* synthesis, originating from hydrogen-bonded interactions, as discussed in the previous section. The average size distribution of the $MoS_2$ grown on the surface of DRH was 183.7 nm (***Figure 4.12*****(g**)). The EDXS analysis of DRH confirms the presence of Si with 11.56 wt.%, along with another constituent C ~53.64 wt.% and O ~34.77 wt.% (***Figure 4.12*****(h**).

EDXS analysis of DRH-$MoS_2$ confirms the presence of Mo with ~23.34 wt.%, with other constituents such as C ~27.02 wt.%, O ~18.78 wt.%, S ~22.23 wt.%, and

inherently presence of Si ~8.54 wt.%, ***Figure 4.12*(i)**. Microscopic analysis of DRH-$MoS_2$ confirms the growth, uniform distribution, and self-assembly of $MoS_2$ nanosheets in cellulose interlayers, making it suitable for pollutant dye remediation, as discussed in subsequent sections.

### 4.3.4 Adsorption of MG on DRH

***Figure 4.13*(a)** shows the adsorption behaviour of DRH at various MG concentrations (100, 200, 400, 600, and 1000 mg/L). The adsorption of MG onto the DRH surface increases steadily over 120 minutes, reaching a plateau of 200 min with a maximum adsorption capacity of 88 mg/g. The highest adsorption percentage was 91 % at 100 mg/L but dropped to 35.2 % at a higher MG concentration of 1000 mg/L. At first, there were unoccupied binding sites for dye molecule attachment, but as they became saturated, the already-filled binding sites could potentially repel incoming ions. Additionally, alterations in the concentration gradient between the solid surface and the solution might have occurred or, due to the presence of available binding sites, led to increased competition among ions, resulting in a stagnation of the adsorption process. Previous research has also reported similar findings, indicating that adsorption may decline as the binding sites become saturated [446].

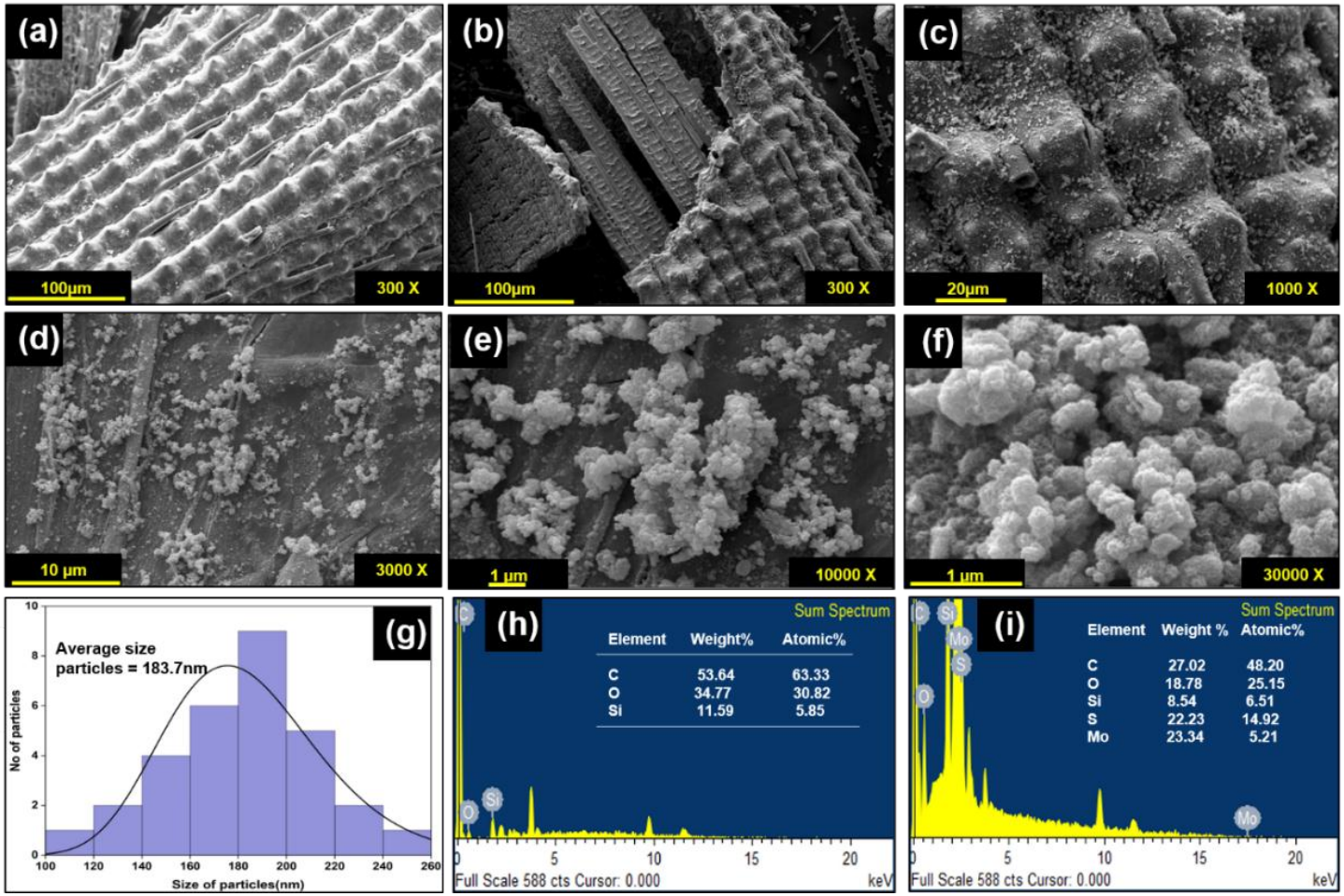


***Figure 4.12*** *SEM-micrograph of (a) DRH and (b) DRH-$MoS_2$, (c) DRH-$MoS_2$ at higher magnification (1000x), dispersed $MoS_2$ nanoflower on DRH (d) at 3000x, (e) 10000x and (f) 30000x magnification, (g) average particle size distribution of $MoS_2$ nanoflowers, EDS spectrograph of (h) DRH, (i) DRH-$MoS_2$*

### 4.3.4.1 Effect of pH and temperature

The effect of temperature on the dye adsorption capacity of DRH was investigated at five different temperatures (30 °C, 35 °C, 40 °C, 45 °C, and 50 °C), as shown in ***Figure 4.13*****(b)**. The percentage of MG adsorption increased consistently with temperature, reaching a maximum of 98.5 % at 50°C, indicating that the adsorption phenomenon is endothermic. The slight increase in the percentage of MG degradation can be accredited to the increased kinetic energy caused by the temperature increase, which improves the mobility and diffusion of dyes to the surface of the adsorbent. This, in turn, promotes increased MG adsorption on the surface of DRH. ***Figure 4.13*****(c)** depicts the effect of pH (3, 5, 7, and 9) on MG adsorption on the surface of DRH. MG adsorption percentage was relatively lower at low pH values, with maximum adsorption (96.2 %) occurring at pH 9. The *pKa* of MG is 4.52, indicating that dye molecules exist predominantly in their cationic form when the pH of the dye is lower than *pKa*. The decreased adsorption at pH 3 is due to the protonation of $H^+$ ions in the solution, which increases the abundance of $H^+$ ions on the DRH surface. Therefore, the positive charge on MG and $H^+$ ions on the DRH surface causes electrostatic repulsion, preventing adsorption. However, as pH rises, the availability of $OH^-$ (deprotonated) on the DRH surface rises, resulting in a decrease in electrostatic repulsion, leading to improved interaction between MG and DRH surface, thus higher adsorption.

### 4.3.4.2 MG adsorption kinetics on DRH

Two kinetic models, the PFO and PSO kinetic models, were fitted to examine the behaviour of adsorption and rate of MG adsorption on the surface of DRH. ***Figure 4.13*****(d)** shows the linear fitting of the PFO kinetics and their parameters mentioned in ***Table 4.11***. The correlation coefficient ($R^2$) values were calculated to be ~0.94-0.99,

indicating that the experimental data best fit the PFO, representing that the MG adsorption on DRH is directly proportional to the number of active sites available. This result suggests that the adsorption of MG on the surface of DRH was predominantly governed by physisorption [449].

***Table 4.11*** *PFO and PSO kinetic parameters for the adsorption of MG onto DRH.*

| **Concentration (mg/L)** | **PFO** | | **PSO** | |
|---|---|---|---|---|
| | $K_1$ | $R^2$ | $K_2$ | $R^2$ |
| 100 | 0.01221 | 0.99 | 0.000872 | 0.88 |
| 200 | 0.00599 | 0.94 | 0.000378 | 0.92 |
| 400 | 0.01245 | 0.98 | 0.003087 | 0.99 |
| 600 | 0.01147 | 0.98 | 0.000162 | 0.77 |
| 1000 | 0.03157 | 0.95 | 0.00024 | 0.81 |

### 4.3.4.3 Adsorption isotherm

To explore the adsorption capacity and the interaction between MG and DRH-$MoS_2$, two widely recognised isotherm models, namely Langmuir (***Figure 4.13*****(e)**) and Freundlich, were examined. These isotherm models provide insights into the distribution of adsorbate on solid adsorbent when equilibrium is reached between the liquid and solid phases of the medium. The experimental adsorption data were fitted to both models and based on the correlation coefficient ($R^2$) values obtained, the Langmuir model ($R^2$ -0.98) is well-suited for studying the removal of dyes using DRH in this study.

This suggests that the adsorption sites on DRH are evenly distributed, and the adsorption process takes place uniformly. The monolayer adsorption capacity ($Q_o$) for the Langmuir isotherm was 80.45 mg/g. The value *1/n* for the Freundlich isotherm was 0.4, less than 1, suggesting that the adsorption phenomenon could have been more

cooperative. The value of n~2.5 observed was more significant than 1, suggesting that the adsorption of MG on DRH is strongly affected by physical adsorption, indicating a favourable influence, as per the Freundlich isotherm.

#### 4.3.4.4 Adsorption thermodynamic

The thermodynamic parameters such as enthalpy ($\Delta H^o$), entropy ($\Delta S^o$), and Gibb's free energy ($\Delta G^o$) were calculated to characterise the adsorption process. A plot of the natural logarithm of the equilibrium constant (*lnKc*) against the inverse of temperature (*1/T*) was used to calculate these values (***Figure 4.13*(f)**). The slope of the plot was used in determining the value of $\Delta H^o$, whereas the intercept provided the value of $\Delta S^o$. The parameter values mentioned in ***Table 4.12*** show that as the temperature rises from 30 to 50°C, $\Delta G^o$ values for MG adsorption on DRH decrease from -2.16 to -10.58 kJ/mol. This decrease suggests MG adsorption on DRH becomes more favourable and spontaneous at higher temperatures [450]. The positive value of $\Delta H^o$ (65.89 kJ/mol) indicates that MG adsorption on DRH is endothermic, requiring energy input for improved adsorption efficiency. Furthermore, a low entropy change ($\Delta S^o$) value (0.22 kJ/K.mol) indicates that DRH has a high affinity for MG with a slight rise in randomness at the interface between DRH and dye solution. However, due to poor adsorption capacity, DRH was chemically modified with $MoS_2$ *via* an *in-situ* hydrothermal process capable of degrading the adsorbed dye available in bulk.

***Table 4.12*** *Adsorption thermodynamic parameters for DRH.*

| Temperature (K) | $\Delta G^o$ ( kJ/mol) | $\Delta S^o$ | $\Delta H^o$ |
|---|---|---|---|
| 303.13 | - 2.16 | 65.89 kJ/mol | 0.22 kJ/K.mol |
| 308.13 | -3.38 | | |
| 313.13 | -6.88 | | |
| 318.13 | -7.19 | | |
| 323.13 | -10.58 | | |

### 4.3.5 Photodegradation of MG under light and adsorption under dark condition by DRH-$MoS_2$

***Figure 4.14*****(a)** shows the catalytic degradation of MG dye at different initial concentrations under both light and dark conditions using a fixed amount of DRH-$MoS_2$. The degradation of MG showed excellent results under light conditions with a removal efficiency of 99 % for dye concentration from 100-1000 mg/L, which reduced to ~84.7 % at a very high MG concentration of 2700 mg/L. The degradation rate was fast within the first five minutes for 100 to 1000 mg/L, with degradation efficiency reaching ~88-90 %. Faster photodegradation of MG using *in-situ* grown DRH-$MoS_2$ might be due to the presence of porous delignified cellulose structures (DRH) and the presence of $MoS_2$ nanoflower, which provides sites for both adsorption of dye and catalytic degradation [451]. At first, MG is adsorbed onto the DRH-$MoS_2$ structures, aiding in the removal of the dye. Subsequently, the photocatalytic properties of $MoS_2$ lead to an improved overall performance [452]. The enhancement of photodegradation by DRH-$MoS_2$ under light conditions can be attributed to the presence of $MoS_2$ in the optical band gaps facilitates the generation of additional electrons and holes when exposed to light [453]. When DRH-$MoS_2$ was subjected to light irradiation, electrons were excited from the valence band to the conduction band, forming holes in the valence band [454–456]. These photo-generated carriers rapidly recombine to form

electron-hole pairs, and their presence on water or oxygen molecules causes the formation of reactive oxygen species (ROS), such as hydroxyl radicals or superoxide radicals. These ROS are critical in degrading organic dyes such as MG by breaking them down into smaller, colourless, and non-toxic molecules. Moreover, the rough surface of DRH and the high volume-to-surface area of $MoS_2$ nanoflowers provide more sites of interaction with photons, resulting in the generation of a large number of ROS. The ROS generated interacts with dye adsorbed onto the cellulose surface in DRH-$MoS_2$ and the MG dye solution, enhancing its degradation. Under dark conditions, the adsorption of MG shows reduced efficiency ranging from ~74-68 % when tested with dye concentrations of 100 to 1000 mg/L. On further increasing the dye concentration to 2700 mg/L at a very high concentration, only 26.6 % adsorption was achieved. The decrease in adsorption efficiency on increasing MG concentration might be due to the absence of ROS reactive species involved in the degradation phenomenon. Therefore, it could be observed that DRH-$MoS_2$ show improved photodegradation (by 25-30 %) with the ability to remove dye even at a high MG concentration of 2700 mg/L, which is typically several orders of magnitude higher than dye levels found in standard industrial wastewater.

#### 4.3.5.1 Effect of pH and temperature on MG degradation

The pH strongly influences dye degradation because it causes protonation or deprotonation with alteration in the surface charge of dye molecules, thereby changing the interaction with the adsorbate. As shown in ***Figure 4.14*****(b)**, the degradation of MG increased with an increase in the pH of the dye solution in both light and dark conditions. The degradation of MG in the presence of light ranged from 63 % to 93 % across pH values ranging from 3 to 11. However, even in the absence of light,

degradation increased from 45 % to 70 % as the pH increased from 3 to 11, albeit at a significantly lower rate than in the presence of light. The catalyst surface becomes protonated at lower pH levels, and MG, a cationic dye, causes electrostatic repulsion, resulting in reduced degradation [457]. As presented in ***Figure 4.14*****(c)**, the degradation of MG (at 300 mg/L) decreases by increasing the temperature in both light and dark conditions. The degradation of MG decreased from 96 to 78 % under light conditions in the temperature range of 30-50°C. Under dark conditions, the percentage of degradation of MG was reduced from 63.3 % to 52.5 % in the temperature range of 30-50 °C. The decrease in the degradation percentage of MG on increasing temperature might be due to a change in the solubility of MG or increased system kinetic energy. The improved kinetic energy of MG molecules may result in their removal from the surface of DRH-$MoS_2$ without being subjected to adsorption, followed by photodegradation [458].

#### 4.3.5.2 Kinetic study of MG adsorption

The PFP and PSO kinetic models were studied to understand the mechanism and adsorption behaviour of MG on DRH-$MoS_2$ (***Figure 4.14*****(d)** and ***Figure 4.14*****(e)).** The PSO kinetic model fitted well with MG photodegradation experimental data, showing good linear behaviour with a coefficient of correlation $R^2$~0.99. The kinetic parameters for PSO and PFO kinetic models are shown in ***Table 4.13*****.** As per PSO kinetics, the adsorption-*cum*-photodegradation of MG dye onto the DRH-$MoS_2$ is controlled by chemisorption. This chemisorption is determined by exchanging or sharing electrons between MG and DRH-$MoS_2$. The kinetic rate constant for PSO kinetic models increased with MG concentration, suggesting that MG molecules adsorbed on the surface of the DRH-$MoS_2$ result in a faster adsorption rate, which is in

line with the experimental studies. The prevalence of such forces with an improved rate of MG dye adsorption onto DRH-$MoS_2$, even at high dye concentrations (~2700 mg/L), led to improved degradation efficiency, making it suitable for industrial-scale wastewater remediation technologies.

#### 4.3.5.3 Continuous photodegradation of MG with DRH-$MoS_2$ and its reusability

A continuous system with dye degradation capabilities makes it easily scalable and translational at an industrial scale with wastewater processing capabilities at higher volume and throughput. The continuous photodegradation experiment using a plug flow reactor (***Figure 4.15*(a)**) was carried out for five cycles, and each cycle continued for 4 hours with 300 mL of MG, illuminated using a 20 W white light source placed at a distance of 15 cm. The maximum degradation of 99.9 % MG was observed in the first cycle, which reduced to 93 % in the second cycle and 82 % and 76 % in the third and fourth cycles, respectively (***Figure 4.14* (f))**. These results show that DRH-$MoS_2$ could continuously degrade 600 mL of MG with more than 90 % efficiency. However, the adsorption capacity of DRH-$MoS_2$ reduced to 52 % after the fifth cycle, possibly due to a reduction in catalytic activity and fewer sites available for the adsorption of MG. This challenge could be overcome by the regeneration of DRH-$MoS_2$ to rejuvenate the catalytically active sites or by increasing the amount of catalyst bed used in the plug flow reactor (only 0.5 g was used in the present study). The above results conclude that DRH-$MoS_2$ could be ideally used for continuous removal of pollutant dye with highly effective degradation capabilities for 5 cycles and microbial decontamination capabilities evaluated in subsequent sections.

***Table 4.13*** *PFO and PSO kinetic parameters of DRH-$MoS_2$ for photodegradation of MG.*

| Concentration (mg/L) | PFO | | PSO | |
|---|---|---|---|---|
| | $K_1$ | $R^2$ | $K_2$ | $R^2$ |
| 100 | 0.06245 | 0.81 | 0.000441 | 0.99 |
| 200 | 0.08172 | 0.87 | 0.008768 | 0.99 |
| 400 | 0.03163 | 0.75 | 0.016214 | 0.99 |
| 600 | 0.04246 | 0.82 | 0.015195 | 0.99 |
| 1000 | 0.07917 | 0.96 | 0.067943 | 0.99 |
| 2700 | 0.05461 | 0.93 | 0.051987 | 0.99 |

### 4.3.6 Free radical scavenging ability of DRH-$MoS_2$

Antioxidant activity refers to a catalyst's ability to counteract damage caused by harmful oxidative stress. This stress arises from increased production of reactive oxygen species (ROS), leading to an imbalance between cellular oxidative processes and antioxidant defences, ultimately resulting in tissue damage. The DRH-$MoS_2$ showed DPPH scavenging activity in the 43.5 % to 74.2 % range for the 0.05 to 0.25 mg/L concentration (***Table 4.14***). These results suggest that the free radical scavenging of DRH-$MoS_2$ increased with the concentration [326,459].

***Table 4.14*** *Represent free radical scavenging activity of DRH-$MoS_2$*

| DRH-$MoS_2$ concentration (mg/L) | DPPH radical scavenging activity (%) |
|---|---|
| 0.05 | 43.52 |
| 0.1 | 49.87 |
| 0.15 | 57.71 |
| 0.2 | 66.75 |
| 0.25 | 74.20 |

### 4.3.7 Antibacterial properties of DRH-$MoS_2$

The antibacterial properties of DRH-$MoS_2$ were studied on *S. aureus* (gram-positive bacteria) and *E. coli* (gram-negative bacteria). The suspension of DRH-$MoS_2$ was gently placed on the freshly cultured plates of *E. coli and S. aureus* using three different DRH-$MoS_2$ concentrations (0.1, 0.2, and 0.5 wt. %). The inhibition zones for the *E. coli* cultured plate were 7, 8, and 8 mm, which slightly increased upon an increase in the concentration of composites. However, in the case of *S. aureus* cultured plate, the inhibition zones were 12, 12, and 13 mm ***Figure 4.15*(b-c)**. The generation of inhibition on both the cultured plates confirms the antibacterial properties of the developed DRH-$MoS_2$. The antibacterial property of DRH-$MoS_2$ might be due to the presence of inherent photocatalytic properties of $MoS_2$ **((*Figure 4.15*(d))**. When $MoS_2$ is directly exposed to light sources, ROS are generated, which aid in destroying or inactivating the microorganisms by the cell membrane lysis [460]. The membrane disruption causes phospholipid extraction and harms the structural integrity of bacteria's lipid membrane. Therefore, the present study provides a unique strategy for RH valorisation through *in-situ* grown $MoS_2$ for simultaneous dye adsorption, photodegradation and microbial decontamination.

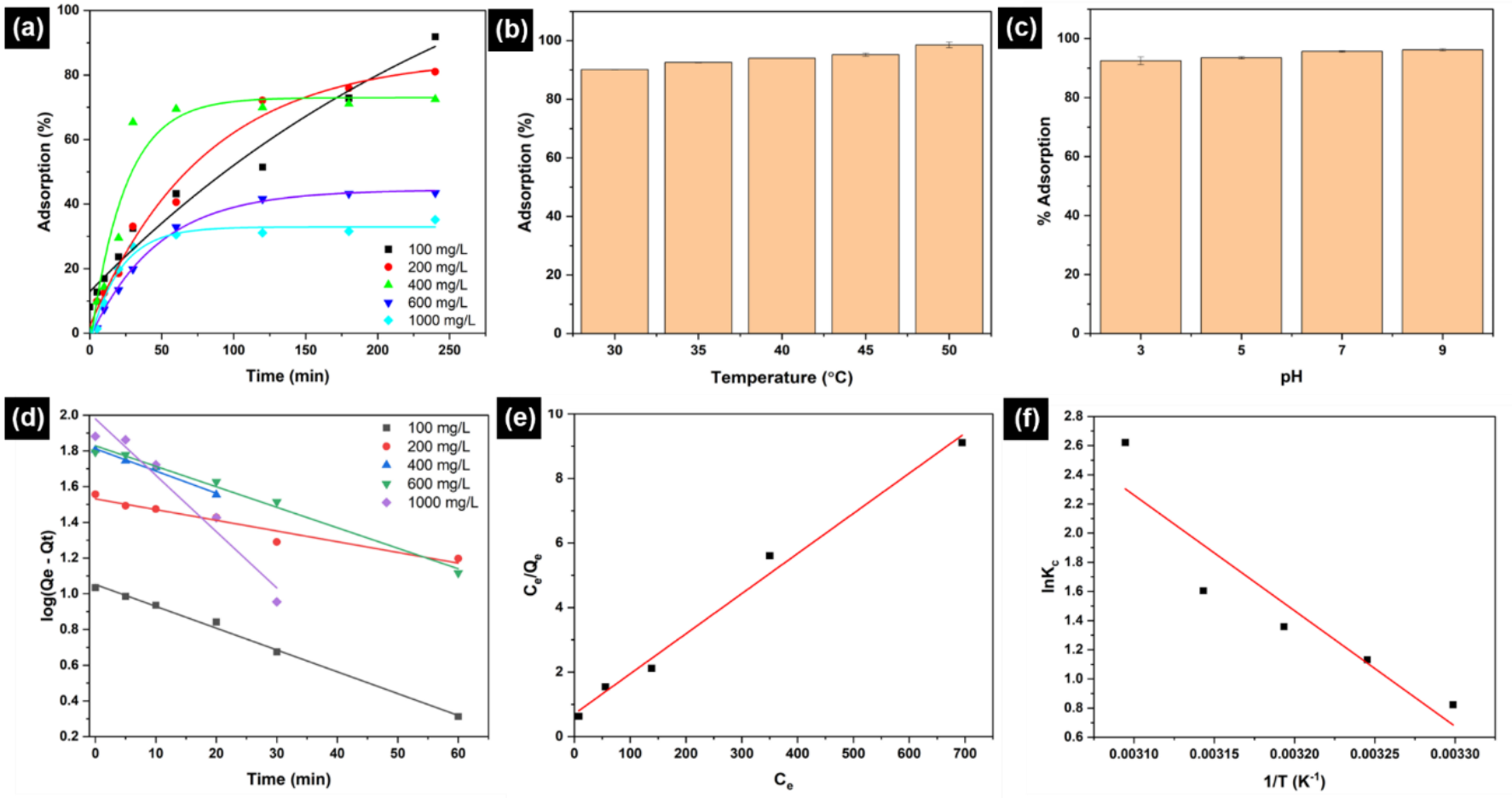


***Figure 4.13*** *Adsorption of MG: (a) % adsorption of MG at various concentrations on DRH at various time intervals, (b) effect of different temperatures, (c) pH on % adsorption of MG, (d) linear fitting of the PFO kinetic model, (e) Langmuir isotherm and (f) studies of adsorption thermodynamic parameters.*

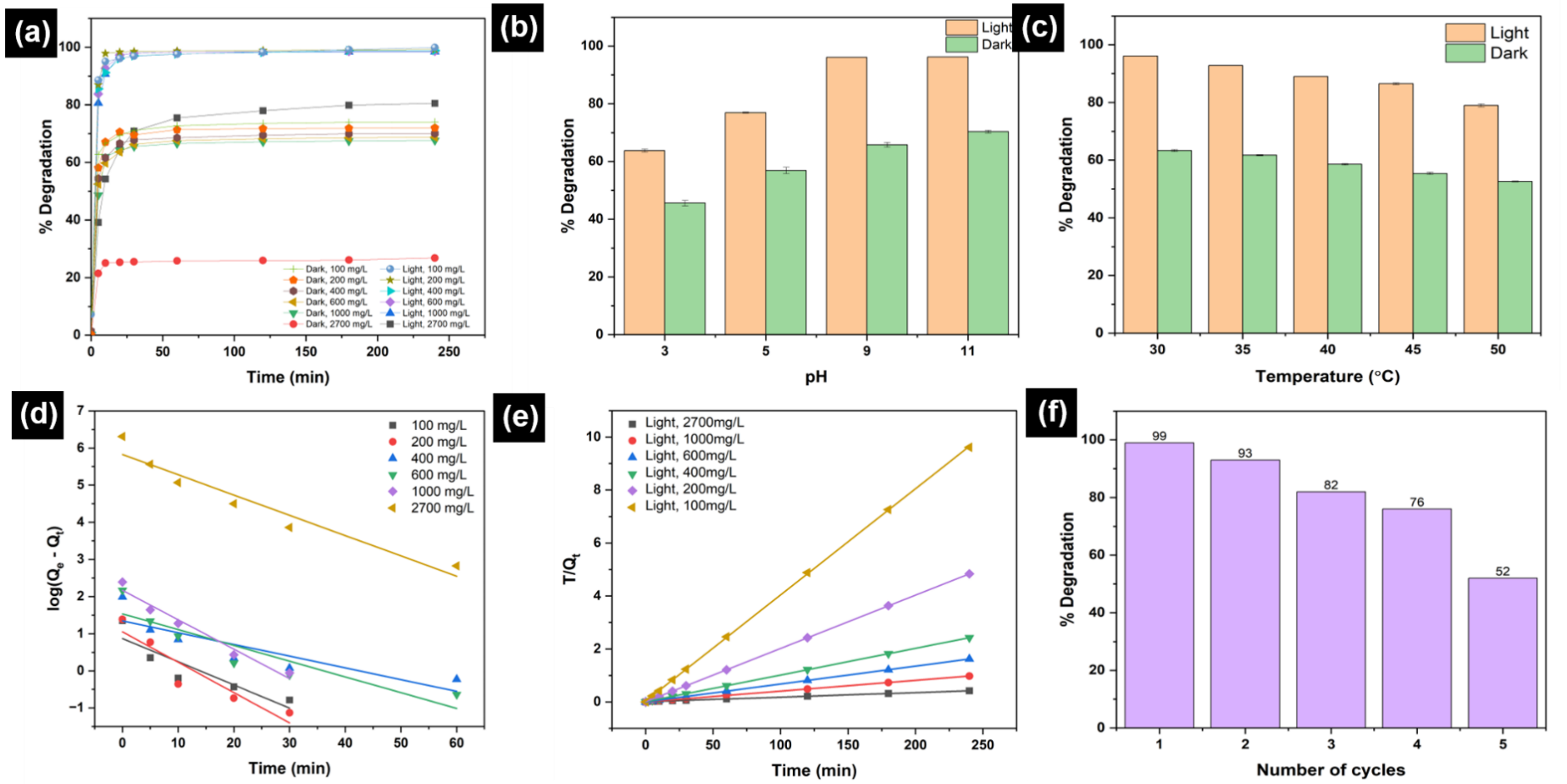


***Figure 4.14*** *Photodegradation of MG by DRH-$MoS_2$: (a) %degradation of MG at various concentrations by DRH-$MoS_2$ in light and dark, (b) effect of pH and, (c) temperature on % degradation of MG, (d) linear fitting of PFO, and (e) PSO kinetic model, and (f) cyclic photodegradation and reusability of DRH-$MoS_2$.*

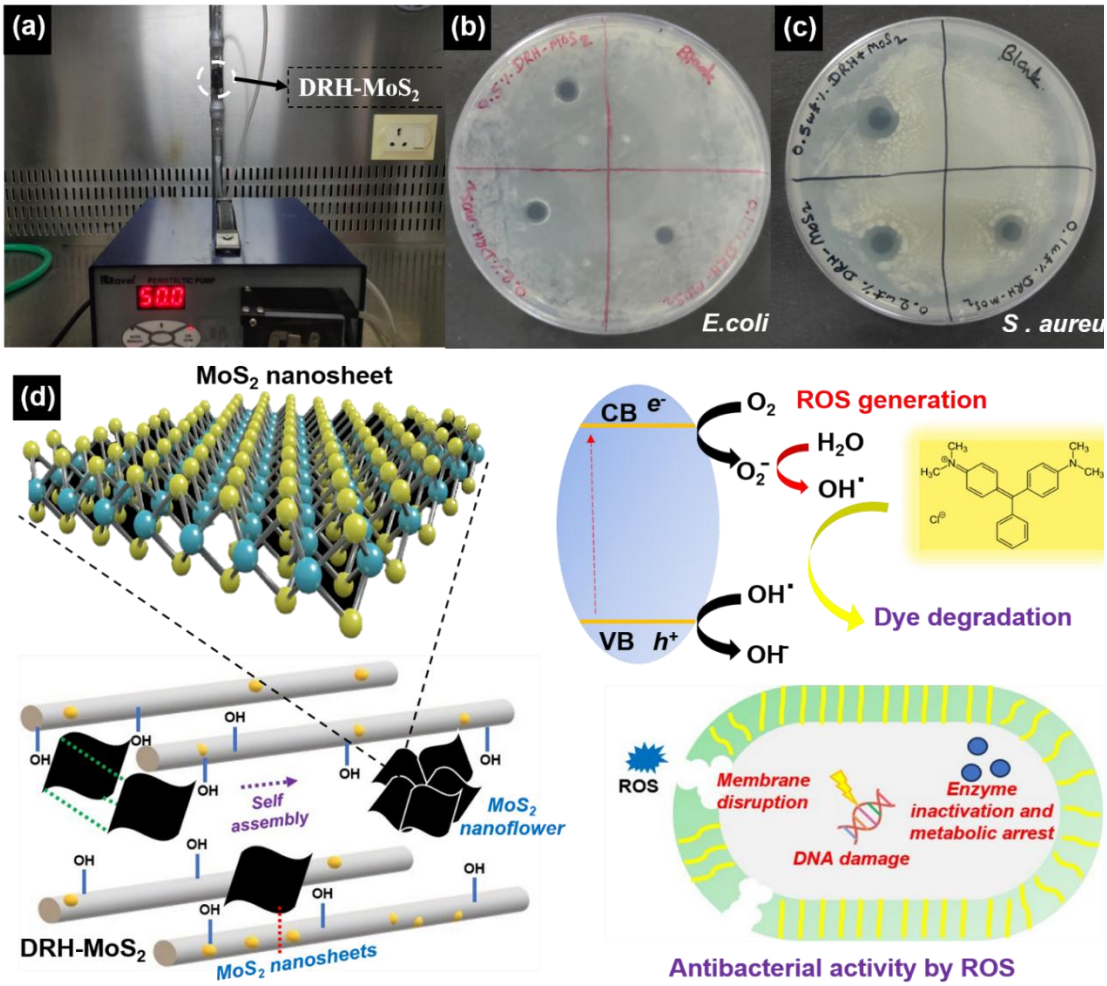


***Figure 4.15*** *Continuous photodegradation of MG and microbial decontamination: (a) plug flow reactor for the continuous photodegradation of MG, (b) antibacterial activities of DRH-$MoS_2$ against E. coli, (c) antibacterial activities of DRH-$MoS_2$ against S. aureus, (d) proposed mechanism for continuous dye degradation and antibacterial properties of DRH-$MoS_2$.*

**4.4 Summary**

In this comprehensive study, rice husk (RH) and sugarcane bagasse (SB), both abundant agro-biomass wastes, were repurposed through a novel approach involving delignification and *in-situ* growth of $MoS_2$. The resulting DRH-$MoS_2$ and DSB-$MoS_2$ composites demonstrated exceptional properties as biocatalysts for wastewater treatment. DSB-$MoS_2$ and DRH-$MoS_2$ exhibited a crystal structure with a hexagonal (*2H*-phase) phase and multi-layered nanosheets structures, forming nanoflower-like structures on the surface. DSB-$MoS_2$ was effective in continuously remediating pollutant dyes like MB and decontaminating microbes in wastewater. Under dark conditions, DSB-$MoS_2$ demonstrated a significant improvement in MB degradation capacity to 114.3 mg/g, further increasing to 158 mg/g in the presence of light. Similarly, DRH-$MoS_2$ exhibited a hexagonal phase with a nanosheet structure, boasting a band gap of 1.37 eV and an impressive 74.2 % capability for scavenging ions. Notably, it showcased outstanding catalytic performance in promoting MG dye adsorption and photodegradation, with efficiency of up to 500 mg/L dye concentration. Furthermore, DRH-$MoS_2$ displayed robust adsorption capacities, particularly under light exposure, reaching 550 mg/g. Both the catalysts demonstrated reusability for three cycles with over 80 % degradation capacity and showcased potent antibacterial responses against *S. aureus* and *E. coli*. This study highlights the sustainable development aspect by transforming agro-biomass waste into valuable materials for high-performance applications in scalable wastewater treatment technologies. These composites solve the disposal problem of these waste materials and remediate dye pollutants and microbiological contaminants in industrial wastewater in a cost-effective and environmentally friendly manner. Repurposing agricultural leftovers is a promise, contributing to a greener, more sustainable circular economy.